

Promising Cathode Materials for Sodium-Ion Batteries from Lab to Application

Shitan Xu,[▽] Huanhuan Dong,[▽] Dan Yang, Chun Wu, Yu Yao, Xianhong Rui, Shulei Chou,^{*} and Yan Yu^{*}



Cite This: *ACS Cent. Sci.* 2023, 9, 2012–2035



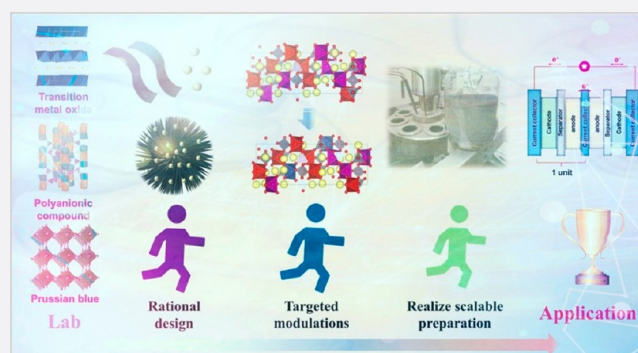
Read Online

ACCESS |

Metrics & More

Article Recommendations

ABSTRACT: Sodium-ion batteries (SIBs) are seen as an emerging force for future large-scale energy storage due to their cost-effective nature and high safety. Compared with lithium-ion batteries (LIBs), the energy density of SIBs is insufficient at present. Thus, the development of high-energy SIBs for realizing large-scale energy storage is extremely vital. The key factor determining the energy density in SIBs is the selection of cathodic materials, and the mainstream cathodic materials nowadays include transition metal oxides, polyanionic compounds, and Prussian blue analogs (PBAs). The cathodic materials would greatly improve after targeted modulations that eliminate their shortcomings and step from the laboratory to practical applications. Before that, some remaining challenges in the application of cathode materials for large-scale energy storage SIBs need to be addressed, which are summarized at the end of this Outlook.



1. INTRODUCTION

Sodium-ion batteries (SIBs) offer safer and more environmentally sustainable solutions to lithium-ion batteries (LIBs) with comparable performance.¹ Despite great potential in applications for high-power energy storage systems, current SIBs still suffer from drawbacks, such as an inferior charge and discharge rate (low power density), lower specific capacity (low energy density), and short cycle life.^{2–4} Cathode materials play a central role in determining the electrochemical performance of SIBs. However, the current SIB cathodes face challenging issues, including undesirable phase changes along cycling, sluggish Na ion mobility, and unfavorable interphase formation between electrode and electrolytes, which are mainly associated with the larger Na ions compared to Li ions.^{5,6} Hence, the selection of electrode materials, especially cathode materials featuring high energy densities and prolonged cycle life, that could buffer the repeated Na⁺ (de)insertion is quite crucial.

Up to now, three categories of materials have been explored as cathodic alternatives for SIBs: transition metal oxides, polyanionic compounds, and Prussian blue analogs (PBAs). Each category of the cathode materials has their own features and inherent problems. The transition layered oxides with large spacers for Na⁺ storage have high reversible specific capacities, high energy densities, and excellent rate capabilities combined with susceptibly convertible technologies. However, such a layered structure is prone to collapse when

accommodating large-radius Na⁺ for (de)insertion, resulting in an unsatisfactory cycle lifespan; besides, most layered oxides are sensitive to the moisture in the air and the absorbent, thus bringing about storage difficulties.^{3,7,8} Polyanionic compounds possess high working voltages and excellent thermal/cyclic stability but suffer from inferior intrinsic electronic conductivity that causes a low specific capacity and poor rate capability.^{9–11} Prussian blue and its analogs have the advantages of low cost, great rate performance, and adjustable working voltage, but the stubborn lattice water is difficult to remove and reduces the chemical stability and structural stability of the PBA material.¹² Effective improvement strategies have been proposed to address the shortcomings of different cathode materials, such as surface modification (isolation or coating), structural design, and lattice or interlayer modulation, in order to realize the high energy density, superior rate capability, and long service lifespan of SIBs (Figure 1).

In this Outlook, we summarized the recent progress of the major cathodic materials for SIBs, introducing their crystal

Received: August 15, 2023

Revised: October 7, 2023

Accepted: October 9, 2023

Published: November 13, 2023



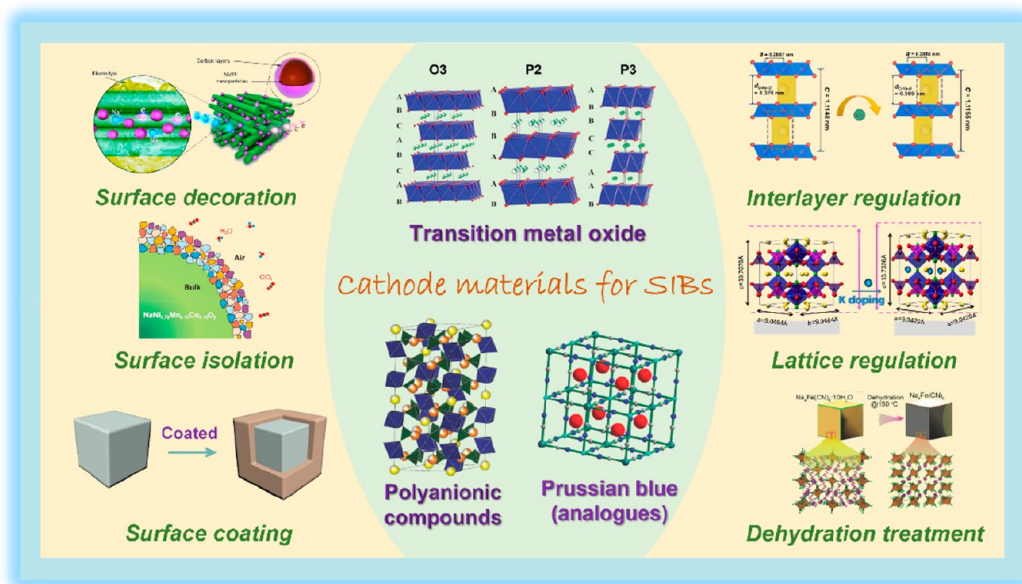


Figure 1. Overview of cathodic materials and their effective modification strategies. Top left image reproduced with permission from ref 182. Copyright 2016 American Chemical Society. Middle left image reproduced with permission from ref 44. Copyright 2018 American Chemical Society. Bottom left image reproduced with permission from ref 138. Copyright Wiley-VCH. Top center image reproduced from 6. Copyright 2020 Wiley-VCH. Bottom-left center image reproduced with permission from ref 12. Copyright 2018 Wiley-VCH. Bottom-right center image reproduced with permission from ref 9. Copyright 2018 Wiley-VCH. Top right image reproduced with permission from ref 68. Copyright 2022 Springer Nature. Middle right image reproduced with permission from ref 183. Copyright 2019 Elsevier. Bottom right image reproduced with permission from ref 184. Copyright 2016 Wiley-VCH.

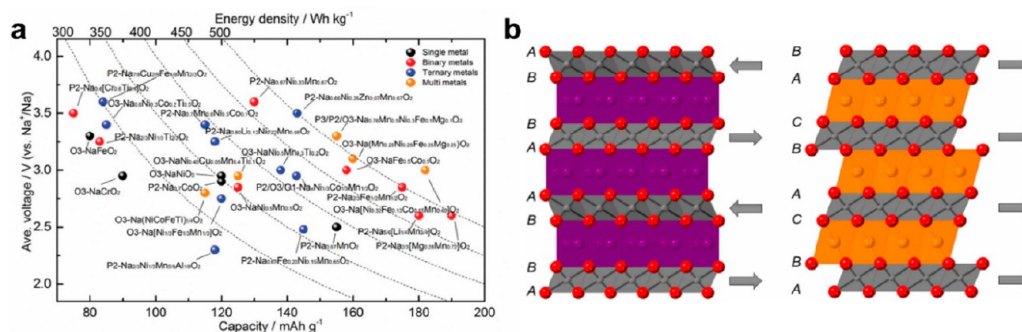


Figure 2. (a) Summary of the electrochemical properties of various layered oxide cathodes. (b) Illustration of P2 (left) and O3 (right) crystal structures. Reproduced with permission from ref 20. Copyright 2021 IOP.

structures, physicochemical properties, and electrochemical applications. Finally, the remaining challenges in the application of these cathode materials for future large-scale energy storage SIBs are discussed. We hope this Outlook can make a guiding contribution to the development of cathode materials for high-energy SIBs.

2. TRANSITION METAL OXIDES

The composition and structure of current cathodes for SIBs are mostly inherited from the LIB cathode analogs, while it is observed that the insertion/alloying of larger Na ions into/with the electrodes leads to distinctive crystal structures, in other words, offering increased structural versatility. In general, the materials that have been investigated as cathodes for SIBs include layered- and tunnel-structured transition metal oxides, polyanion compounds, and Prussian blue analogs (PBAs). Among them, layered transition metal oxides are considered as the most important cathodic alternatives for SIBs. Figure 2a compares the voltages, capacities, and energy densities of the

layered metal oxide cathodes composed of single, binary, ternary and multicomponent metal ions. Typical Na-based layered transition oxides, i.e., NaMO_2 ($M = \text{Ni, Co, Mn, Fe, Cr, V, etc.}$), exist in different crystal structures denoted as P2, P3, O2, and O3 according to Delmas' notation.¹³ O and P indicate the coordination environment of Na^+ , in which O represents the Na occupancy at the octahedron sites surrounded by six oxygens and P represents the Na occupancy at the center of prism sites surrounded by six oxygens. Among them, O3-phase and P2-phase are most widely investigated as cathodes for SIBs, and their crystal structures are illustrated in Figure 2b. Typical examples of O3-type metal oxides include NaFeO_2 ,¹⁴ NaNiO_2 ,¹⁵ and $\text{NaNi}_{1/2}\text{Mn}_{1/2}\text{O}_2$,¹⁶ and those for P2-type metal oxides include $\text{Na}_{2/3}\text{MnO}_2$,¹⁷ $\text{Na}_{0.7}\text{CoO}_2$,¹⁸ and $\text{Na}_{2/3}\text{Ni}_{1/3}\text{Mn}_{2/3}\text{O}_2$.¹⁹ Generally, the P2 structure renders the best power performance for SIBs, as Na ion diffuse through rectangular faces between adjacent trigonal prismatic environments, which is unavailable in LIBs. The O3-structured materials are outstanding in capacity, as they have the highest

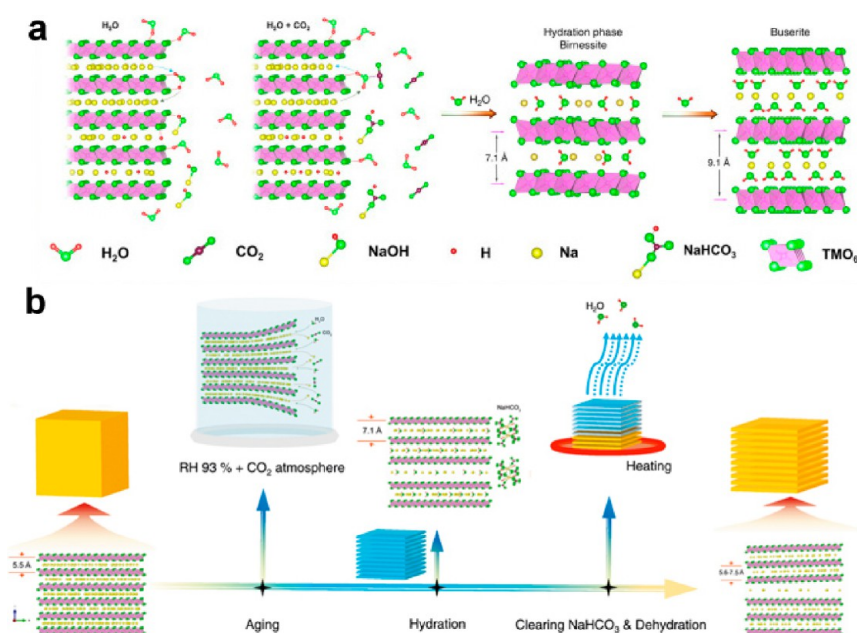


Figure 3. (a) Schematic illustration of the hydration and CO₂ uptake process when exposing layered metal oxides in air. Reproduced with permission from ref 51. Copyright 2023 American Chemical Society. (b) Water-mediated synthetic process that can expand the interlayer spacing between the Na⁺ layers. Reproduced with permission from ref 54. Copyright 2021 Springer Nature.

sodium stoichiometries. In recent years, hybrid P2/O3-structured materials have attracted extraordinary attention for simultaneous optimization of the power and energy density for SIBs.

2.1. Na-Free Transition Metal Oxides. Vanadium oxides have been investigated as the cathodic materials for SIBs due to their features of high capacity and low cost. VO₂(A) is unstable during electrochemical reactions,²¹ but VO₂(B) is considered a more suitable cathode for SIBs because its layered structure allows for rapid Na ion diffusion; the corresponding theoretical capacity is as high as 322 mA h g⁻¹, which is associated with one e⁻ transfer during the (de)sodification process.^{22,23} However, VO₂(B) is metastable and less conductive, so rapid capacity fading was often observed for VO₂(B) because of the drastic volume expansion, dissolution, and aggregation of the electrode material. In comparison, V₂O₅ shows higher chemical and thermal stability with layered and orthorhombic structures, both of which are electrochemically active. The theoretical capacity of V₂O₅ varies depending on the number of transfer electrons involved in the redox reaction (capacities of 294 and 441 mA h g⁻¹ corresponding to 2e⁻ and 3e⁻ participating in the reaction, respectively). The electrochemical process of V₂O₅, however, starts to degrade with the morphology change or crystal structure collapse upon cycling, which is also known as “lattice breathing”.²⁴ The stability of V₂O₅ electrodes can be enhanced by inserting larger cations (Na⁺, NH₄⁺) or water molecules into the crystal interlayers.^{25,26,27} Constructing V₂O₅ aerogels with highly porous 3D networks has also proved to be an efficient strategy for enhancing their performance.²⁸ Apart from the crystallized structure, the amorphous V₂O₅ also demonstrates a Na storage property.²⁹ Furthermore, manganese oxides, such as α-MnO₂ and β-MnO₂, show promise as cathodes for SIBs, and they exhibit a theoretical Na⁺ storage capability of 308 mA h g⁻¹.³⁰ In particular, the compact tunnels in β-MnO₂ along the [001] direction are favorable for the Na⁺ insertion/extraction and contribute to the better Na storage capacity. Introduction of

exchangeable guest cations into the MnO₂ framework can modulate the Na storage performance, though the exact role and effects of the guest ions still needs further investigation.³¹

2.2. Layered Sodium Monometallic Oxides. The sodium monometallic oxides often suffer from poor stability and rapid degradation due to the continuous phase changes of the oxides, especially at high voltages. For example, α-NaFeO₂ is a O3-type cathode material with excellent thermal stability with an active Fe³⁺/Fe⁴⁺ redox couple. Under higher voltages, their electrochemical performance degrades mainly due to the Jahn–Teller distortion and polarization. Fe⁴⁺ is reduced to Fe³⁺ at the charged state, and the excessive Fe³⁺ will migrate and block the diffusion pathways of Na ions, causing the degradation of performance.³² A recent finding also points out both oxygen reactivity and the Fe³⁺/Fe⁴⁺ contribute to the electrochemical activity of NaFeO₂, evidenced by the diminished Fe³⁺ ions under high voltages.³³ Partially substituting Fe with Ni³⁺ ions or Co³⁺ ions, reducing the particle sizes, or surface modification can help enhance the stability of NaFeO₂.³⁴ Na_xCoO₂ exists in both the P2 and O3 phase, where the P2 phase is relatively more stable without gliding of the CoO₆ slabs during the charge and discharge process.^{35,36} The stability of this material is mainly affected by the Na⁺/vacancy ordering, which can be relieved by partial substitution of the Co ions with Ni³⁺, Mn²⁺, and Ti⁴⁺.^{36,37,38} Similar to MnO₂, Na_xMnO₂ suffers from severe volume change induced by the Jahn–Teller distortion and dissolution of Mn species during the electrochemical reactions.^{39,40} The disproportionation of Mn³⁺ into Mn⁴⁺ and Mn²⁺ results in the dissolution of Mn species into the electrolyte. High-temperature quenching can remove the Mn vacancies and suppress their dissolution, while also creates more Mn³⁺ and leads to more severe Jahn–Teller distortion.¹⁷ An alternative strategy is to quench the electrode using liquid N₂ which can eliminate the Mn vacancies without creating extra Mn³⁺ ions.⁴¹ Although Ni has been widely used as a doping metal, Na_xNiO₂ electrodes show inferior performance and poor stability when

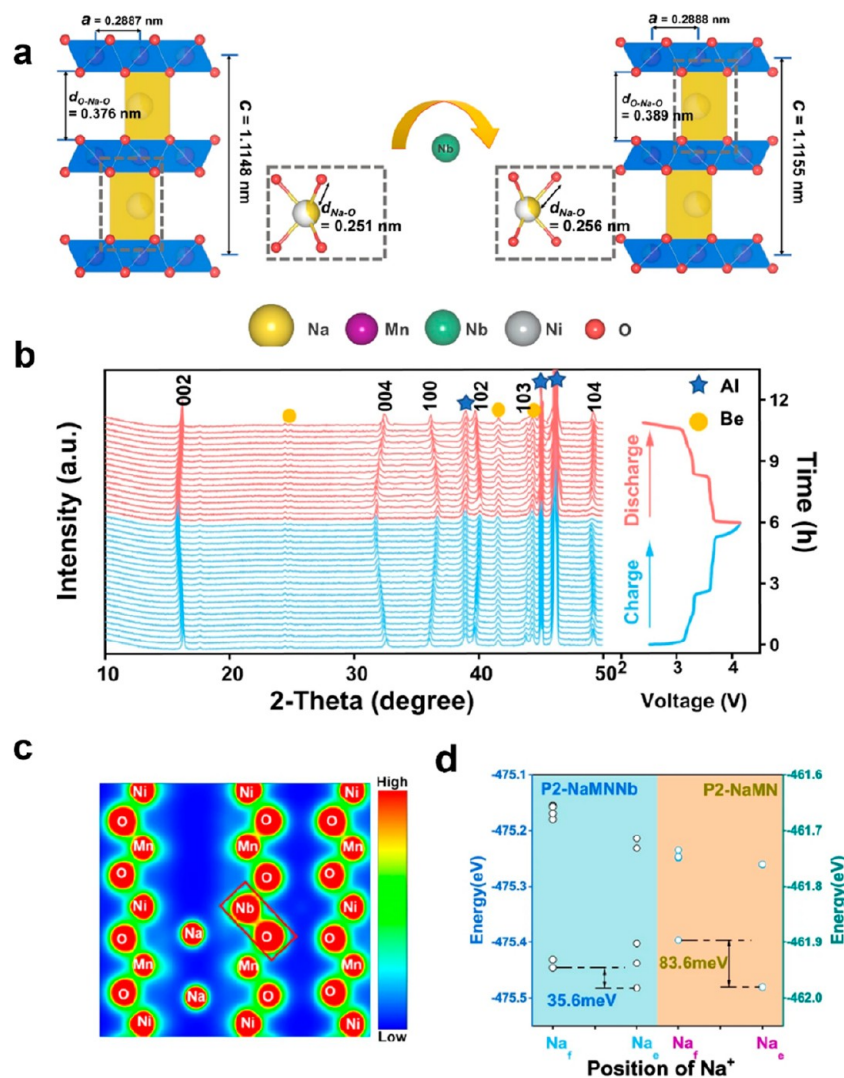


Figure 4. (a) Variation of the crystal structures in $\text{Na}_{2/3}\text{Mn}_{2/3}\text{Ni}_{1/3}\text{O}_2$ with Nb doping. (b) In situ XRD patterns of the electrodes during the charge and discharge process. (c) Charge density distribution in the Nb-doped $\text{Na}_{2/3}\text{Mn}_{2/3}\text{Ni}_{1/3}\text{O}_2$. (d) Calculated energy difference between different Na sites with and without Nb doping. Reproduced with permission from ref 68. Copyright 2022 from Springer Nature.

used as cathodes for SIBs. Decay of a high-Ni cathode is mainly associated with the insertion of water and carbonate ions between the TMO₂ slabs and oxidation of the electrodes.^{42–44} Washing with ethanol, reducing interlayer spacing, and using proper electrolyte are effective strategies to enhance their stability.⁴⁵ NaVO_2 shows a similar structure to O3 $\alpha\text{-NaFeO}_2$, while the pure-phase NaVO_2 is difficult to synthesize. NaVO_2 can only be reversibly cycled in the narrow working window of 1.4–2.5 V.⁴⁶ When a higher voltage was applied, the composition underwent continuous variation with the emergence of many potential plateaus. NaCrO_2 has a theoretical capacity of $\sim 250 \text{ mA h g}^{-1}$, but it faces a similar issue of poor irreversibility at high voltages, just like NaVO_2 .⁴⁷ It has been reported that partial substitution of Cr by Ru and Ca ions can be effective in obtaining a more stable NaCrO_2 electrode.^{48,49} The Ru substitution can possibly improve the working plateau (presenting an extra high voltage plateau at 3.8 V) and shows an excellent cycling performance (80.7% capacity retention after 1100 cycles). When Ca is doped in NaCrO_2 , it can improve the cycling performance (76% for 500 cycles) and air stability (slight change observed after exposure for a month). For layered sodium monometallic oxides,

element doping is primarily applied to restrict the influence of Na^+ /vacancy ordering and the Jahn–Teller effect in Na_xMO_2 ($M = \text{Fe}, \text{Co}, \text{Mn}, \text{Ni}, \text{etc.}$), as well as to improve the structural stability (air-stability). In this regard, some inactive elements such as Ti, Ru, and Ca have shown effective results in improving the aforementioned effects.

Another challenge with the layered metal oxides is their hygroscopic nature, as they tend to uptake water and CO_2 from air, which results in fast capacity decay and dissolution of the electrodes (as illustrated in Figure 3a).^{42,50,51} Surface modification by coating ZrO_2 , Na_2TiO_7 , or AlF_3 can be effective in promoting ion diffusion, enhancing air stability, and preventing infiltration of the electrolyte, therefore improving the stability of the cathode materials.^{44,52,53} The hygroscopic nature of Na_xMnO_2 has been utilized to expand the interlayer spacing between Na layers, which can facilitate the Na ion transport and suppress the phase transformations during the electrochemical reactions. As illustrated in Figure 3b, the continuous aging and hydration process allows full uptake and insertion of CO_2 and water molecules, leading to significantly enlarged Na^+ layer spacing in the $\text{P2-Na}_{0.67}\text{MnO}_2$.⁵⁴

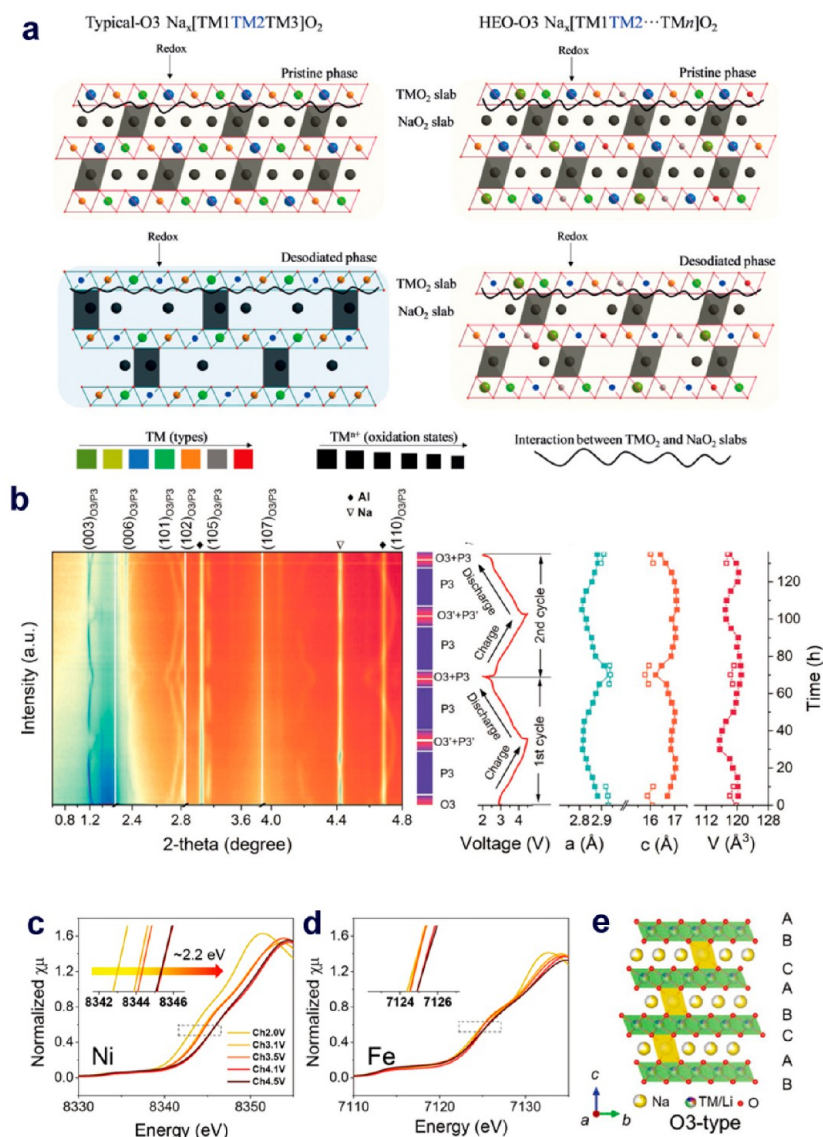


Figure 5. (a) Illustration of the mechanisms of traditional metal oxides and multicomponent HEO in stabilizing the O3-type structure. Reproduced with permission from ref 70. Copyright 2019 Wiley-VCH. (b) In situ high-energy XRD patterns during the first charge–discharge cycles of $\text{Na}_{2/3}\text{Li}_{1/6}\text{Fe}_{1/6}\text{Co}_{1/6}\text{Ni}_{1/6}\text{Mn}_{1/3}\text{O}_2$ cathode. XANES spectra of the (c) Ni K edge and (d) Fe K edge. (e) O3-structure with a superlattice. Reproduced with permission from ref 71. Copyright 2022 Wiley-VCH.

2.3. Layered Sodium Multimetallic Oxides. Nowadays, most of the research attention has been devoted to the development of multimetallic oxide cathodes for high-performance SIBs. With the cooperative benefits from different metal ions, the common issues encountered by the monometallic oxide cathodes, such as the Jahn–Teller distortion, undesired Na^+ /vacancy ordering, and structural instability, can be effectively addressed. Substituting Mn ions with Cu^{2+} ions can modulate the air and water sensitivity of Na_xMnO_2 .⁵⁵ Partial substitution of Cr^{3+} with Ti^{4+} in $\text{Na}_{2/3-x}\text{Cr}_{2/3}\text{Ti}_{1/3}\text{O}_2$ endowed the electrode with a higher operating voltage.⁵⁶ The presence of Ru in the $\text{Na}_{0.88}\text{Cr}_{0.88}\text{Ru}_{0.12}\text{O}_2$ suppressed the irreversible migration of Cr ions and elevated the operating voltage.⁴⁸ In particular, forming a O3/P2 hybrid structure has become a popular strategy to achieve cathode materials with both high capacity and high stability. Typical O3/P2 hybrids include the O3-type $\text{NaNi}_{0.5}\text{Mn}_{0.5}\text{O}_2$ mixed with minor P2 phases, such as $\text{Na}_{0.66}\text{Li}_{0.18}\text{Mn}_{0.71}\text{Ni}_{0.21}\text{Co}_{0.08}\text{O}_2$,⁵⁷

$\text{Na}_{0.67}\text{Mn}_{0.55}\text{Ni}_{0.25}\text{Ti}_{0.2-x}\text{Li}_x\text{O}_2$,⁵⁸ and $\text{Na}_x[\text{Ni}_{0.2}\text{Fe}_{x-0.4}\text{Mn}_{1.2-x}]\text{O}_2$ ($x = 0.7-1.0$).⁵⁹ These hybrid-structured electrodes generally showed smoother charge–discharge profiles, reduced polarizations, and higher capacities during the cycling process.

Metal substitution is effective in suppressing the phase transition during the reaction process. For example, Al and Fe substitution can suppress the undesired phase transition in $\text{Na}_{0.67}\text{Al}_{0.1}\text{Fe}_{0.05}\text{Mn}_{0.9}\text{O}_2$.⁴¹ The Jahn–Teller distortion in Na_xMnO_2 can be suppressed by the introduction of Li^+ , Mg^{2+} , Fe^{3+} , Ni^{3+} , and Ti^{4+} ions.^{60,61} The reason for Li^+ and Mg^{2+} substitution is that they can oxidize Mn^{3+} into Mn^{4+} and thus reduce the Jahn–Teller distortion.^{62,63} Besides cation doping, doping with fluorine has lowered the energy barrier for Na ion diffusion in $\text{Na}_{0.46}\text{Mn}_{0.93}\text{Al}_{0.07}\text{O}_{1.79}\text{F}_{0.21}$.⁶⁴ A honeycomb-ordered O3– $\text{Na}_3\text{Ni}_2\text{Sb}_6\text{O}_6$ has demonstrated a high capacity and stability upon cycling.⁶⁵ The enhanced stability originated from the presence of the honeycomb-ordered Ni_2SbO_6 slabs. Substituting 1/3 of Ni with Sb led to the

formation of the Ni₆-ring structure inside NaNiO₂, which degenerated the electronic orbitals and increased the redox potential of the cathode. Partial substituting Ni²⁺ with inactive cations such as Zn²⁺, Mg²⁺, and Ca²⁺ resulted in the formation of the nanodomains composed of intergrown P3–O1 phases within the crystal structure of Na_{0.2}Ni_{0.45}Zn_{0.05}Mn_{0.4}Ti_{0.1}O₂, which not only fully strengthened the potential capacity of the metal oxide electrode but also suppressed the undesired phase transition and structural degradation upon cycling.⁶⁶ Potassium ions were introduced into the P2–K_{0.5}Mn_{0.7}Fe_{0.2}Ti_{0.1}O₂ and served as pillar ions to expand the lattice for Na ion insertion and deinsertion and stabilize the crystal structure.⁶⁷

To address the irreversible structural changes or phase transitions of P2–Na_{2/3}Mn_{2/3}Ni_{1/3}O₂ aroused by severe interfacial transition and metal dissolution, Nb-doped P2–Na_{0.78}Ni_{0.31}Mn_{0.67}Nb_{0.02}O₂ with proper surface modifications enabled fast Na⁺ (de)intercalation for efficient battery cycling even at low temperatures such as –40 °C, showing a high specific capacities of 83.6 and 62.9 mA h g^{–1} at 920 and 1.84 A g^{–1}, respectively. Besides, superior long-term cyclability at low temperatures is demonstrated by the high capacity retention of 76% at 368 mA g^{–1} over 1800 cycles.⁶⁸ As shown in the refined crystal structure in Figure 4a, Nb doping can expand the spacing between the TM layers from 0.376 to 0.389 nm and extend the Na–O bond from 0.251 to 0.256 nm, endowing Na⁺ with enhanced (de)intercalation capabilities. The in situ X-ray diffraction (XRD) spectra shown in Figure 4b illustrate that all the characteristic diffraction peaks revert to their original initial positions without the appearance of any new phase after a charge/discharge cycle. The charge density distribution of the Nb-doped Na_{2/3}Mn_{2/3}Ni_{1/3}O₂ reflects that the interaction between TM and O is more intense than that between Na and O (Figure 4c), and the energy calculation implies that the Na hopping is easier when Nb is doped in (Figure 4d).

2.4. Novel Metal Oxide Cathodes. Apart from the conventional layered metal oxides cathodes, metal oxides cathodes that adopt novel compositions and crystal structures or employ a novel Na storage mechanism has also been explored. Middle-entropy oxides (MEOs) and high-entropy oxides (HEOs) are novel categories of multimetallic single-phase solid solution oxides with multiple metals sharing the crystallographic sites and stabilizing the host structure through the “entropy-stabilization effect”.⁶⁹ In addition, the oxygen vacancies generated among the metal ions can effectively promote the Na ion diffusion. For example, the multicomponent in O3-type Na–Ni_{0.12}Cu_{0.12}Mg_{0.12}Fe_{0.15}Co_{0.15}Mn_{0.1}Ti_{0.1}Sn_{0.1}Sb_{0.04}O₂ results in different local interactions between elements in TMO₂ slabs and Na in NaO₂ slabs and achieves entropy stabilization on the host (illustrated in Figure 5a),⁷⁰ which has suppressed the phase transition and benefited the long-term cycling of the high-entropy metal oxides electrodes.

A high-entropy Na_{2/3}Li_{1/6}Fe_{1/6}Co_{1/6}Ni_{1/6}Mn_{1/3}O₂ cathode with a superlattice structure with Li/transition metal ordering presented excellent electrochemical performance.⁷¹ The as-prepared cathode shows high reverse capacities of 172.3 mA h g^{–1} in the first cycle at 0.1 C and 78.2 mA h g^{–1} at 10 C, demonstrating its superior rate capacity. Excellent cycling stability with the retention of 63.7% after 300 cycles at a current density of 5 C was also validated. In situ high-energy XRD confirmed the O3-type structure of the original cathode, which underwent a fast O3–P3 phase transition at the initial

stage of charging (Figure 5b). X-ray absorption spectroscopy (XAS) analysis (Figure 5c, d) reveals that the Ni²⁺/Ni³⁺/Ni⁴⁺ and Fe³⁺/Fe⁴⁺ redox couples jointly contributed to the high reversible capacity, while Co doping enhanced the electronic conductivity. Moreover, the superlattice structure of the electrode maintained stable even after long cycles, as illustrated in Figure 5e.

Another emerging type of cathode material is metal oxides involving anionic redox reactions (ARRs) for ion storage. Some of the metal oxides are anionic redox-active intrinsically. For example, NaVO₃ and Na₃RuO₄ are intrinsic ARR materials with both cathodic and anionic redox couples that contribute to the high capacity.^{72,73} With proper engineering over the structure and composition, ARR electrodes can be created through metal ion doping. The Zn-doped P2–Na_{2/3}Mn_{1–y}Zn_yO₂ electrode showed high oxygen redox activity associated with nonbonding O(2p) orbitals.⁷⁴ Doping metal ions causes ionic bonding, such that the electrons fully localized on the oxygen anions and the TM deficiency were the key to activate the oxygen anion redox activity. Metal ions that can form ionic bonds with oxygen, e.g., Li–O, Na–O, and Mg–O bonds, can be doped to create O(2p) nonbonding orbitals so that the electrons are fully localized on the oxygen anions. On the other hand, the P2 structure in ARR Na_{0.72}[Li_{0.24}Mn_{0.76}]O₂ could be stabilized even when 0.93 Na was extracted.⁷⁵ The change in the oxygen radii and charges carried by the oxygen ions resulted in a decrease in oxygen repulsion around the empty Na layer and hence stabilized the structure. Besides, with the double redox reaction from both Ni²⁺/Ni⁴⁺ and O^{2–}/O^{n–}, the higher redox potential of Na[Mn_{0.5}Ni_{0.5}]O₂ compared to that of NaMnO₂ with a single redox reaction was expected.⁷⁶ However, it was also noticed that the ARR electrodes suffer from the structural degradation in complex phase transitions and loss of oxygen during the cycling process.

2.5. Scalable Preparation of Transition Metal Oxides.

The reports on the scalable preparation of transition metal oxides mainly center on the coprecipitation method. It has the ability to achieve layered oxide cathode materials with a smooth surface, uniform particle size distribution, and high compaction density by controlling reaction conditions, making this method more suitable for industrial production. Sun and coworkers proposed a nickel-rich Na(Ni_{0.65}Co_{0.08}Mn_{0.27})O₂ material with a core–shell structure, which was prepared through coprecipitation followed by milling at a rotational speed of 1000 r min^{–1} at 50 °C.⁵² Its first discharge specific capacity was 168 mA h g^{–1} measured at 0.5 C within the voltage range of 1.5–4.0 V, and the capacity retention rate after 50 cycles was found to be 77%. Ding et al. synthesized a novel Ni-rich O3-type Na[Ni_{0.60}Fe_{0.25}Mn_{0.15}]O₂ cathode for SIBs via the industrially feasible hydroxide coprecipitation method followed by high-temperature calcination.⁷⁷ By reducing the charge voltage from 4.2 to 4.0 V (i.e., eliminating the high-voltage O3'' phase), the electrode exhibited an excellent overall performance, including the high reversible capacity of 152 mA h g^{–1} and a superior capacity retention of ~84% after 200 cycles at 0.5 C.

3. POLYANIONIC COMPOUNDS

Among various cathode materials, the polyanionic-type cathodes also attract much attention due to their high working potential and great structural stability. The general formula of polyanionic-type cathode materials in SIBs is NaM_x(XO_y)_z.

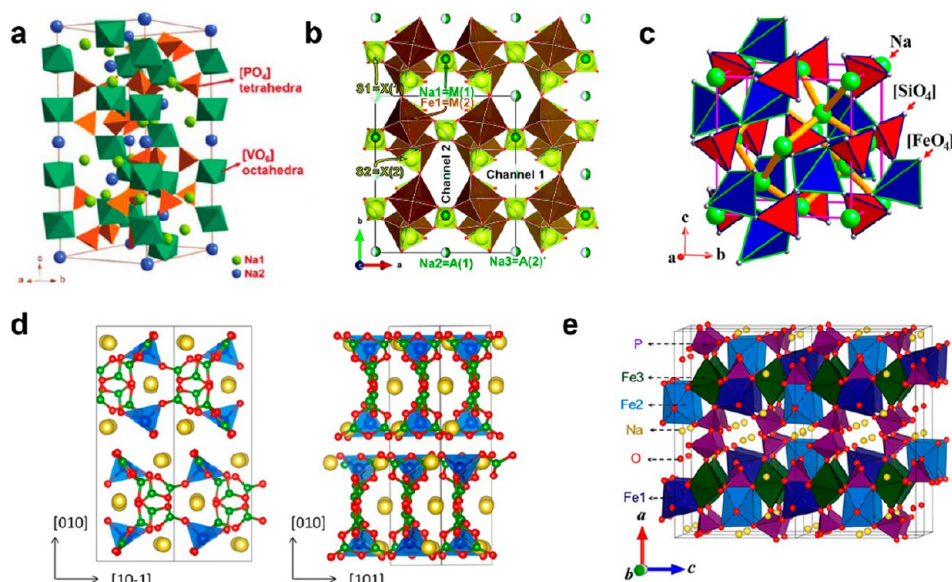


Figure 6. (a) Crystal structure of $\text{Na}_3\text{V}_2(\text{PO}_4)_3$. Reproduced with permission from ref 87. Copyright 2019 Royal Society of Chemistry. (b) Crystal structure of $\text{Na}_2\text{Fe}_2(\text{SO}_4)_3$. Reproduced with permission from ref 88. Copyright 2019 Royal Society of Chemistry. (c) Crystal structure of $\text{Na}_2\text{FeSiO}_4$. Reproduced with permission from ref 82. Copyright 2016 American Chemical Society. (d) Crystal structure of $\text{Na}_3\text{FeB}_5\text{O}_{10}$. Reproduced with permission from ref 83. Copyright 2016 American Chemical Society. (e) Crystal structure of $\text{Na}_4\text{Fe}_3(\text{PO}_4)_2(\text{P}_2\text{O}_7)$. Reproduced with permission from ref 89. Copyright 2012 American Chemical Society.

$n\text{H}_2\text{O}$, where M represents a transition metal element, such as V, Fe, Mn, Cr, Ni, Ti, etc., and X is nonmetal element like P, S, Si, As, Mo, or W.^{9,10} According to the different type of polyanion, polyanionic cathode can be divided into the following categories: phosphate, sulfate, silicate, borate, and mixed-polyanion materials. The high induction effect brought by the polyanionic XO_4 can effectively increase the working voltage of the cathode, and the polyhedral connection of XO_4 and MO_6 makes the structure stable, which can withstand repeatedly Na^+ (de)insertion, prolonging the working life of the batteries.⁷⁸ Nevertheless, polyanionic materials also face certain problems, including intrinsically inferior electronic conductivity, causing lower specific capacity and poor rate performance. In order to solve these problems, it is essential to have a comprehensive understanding of polyanionic materials, ranging from the crystal structures, their basic physicochemical properties, the Na storage mechanism, and current advances of polyanionic cathodes for SIBs.

3.1. Characteristics of Polyanionic Compounds.

3.1.1. Phosphates. The phosphate-based materials in SIBs can be divided to three categories: orthophosphate NaMPO_4 ($M = \text{Fe, Mn, Ni}$), NASICON-type $\text{Na}_x\text{M}_y(\text{PO}_4)_3$ ($M = \text{V, Fe, Mn, Ti}$), and pyrophosphate $\text{Na}_2\text{MP}_2\text{O}_7$ ($M = \text{V, Fe, Co, Mn}$).⁷⁹ As a representative of NaMPO_4 , the crystal structures of NaFePO_4 are mainly olivine type (o- NaFePO_4) and maricite type (m- NaFePO_4). o- NaFePO_4 consists of FeO_6 octahedra and PO_4 tetrahedra forming a spatial skeleton, with Na^+ occupying the cosided octahedra and forming a long chain along the b -axis direction (its theoretical capacity is 156 mA h g^{-1} based on $2e^-$ transportation); in contrast, the positions of Na^+ and Fe^{2+} in m- NaFePO_4 are reversed and the position of PO_4^{3-} remains unchanged, blocking the Na^+ diffusion channel and resulting in poor or even inactive electrochemical performance. With the structural stability of m- NaFePO_4 , methods for stimulating its electrochemical activity are being continuously studied. As shown in Figure 6a, the classical

NASICON-type $\text{Na}_3\text{V}_2(\text{PO}_4)_3$ belonging to $\text{Na}_x\text{M}_y(\text{PO}_4)_3$ ($M = \text{V, Fe, Mn}$) has two MO_6 octahedra and three PO_4 tetrahedra sharing oxygen atoms for linkage, with the Na^+ occupying two unequal Wyckoff sites, one Na^+ at the 6b site (M1) and the other at the 18e site (M2). The pyrophosphate-type materials are represented as $\text{Na}_2\text{MP}_2\text{O}_7$ ($M = \text{V, Fe, Co}$), with $\text{P}_2\text{O}_7^{5-}$ having a higher inductive effect than PO_4^{3-} that can greatly increase working voltage. In the crystal structure of $\text{Na}_2\text{FeP}_2\text{O}_7$, the Fe_2O_{11} copolymer connected by two FeO_6 octahedra coangularly and P_2O_7 connected by two PO_4 tetrahedra coangularly are bridged together in a coedge or coangle to form a 3D twisted zig-zag-type Na^+ transport channel, and five Na sites with different occupancy degrees are generated. The redox reaction of $\text{Fe}^{2+}/\text{Fe}^{3+}$ occurs at a suitable voltage window for the reversible extraction/insertion corresponding to one Na^+ with a theoretical specific capacity of 97 mA h g^{-1} , and two clear plateaus of 2.5 and 3.0 V can be observed.

3.1.2. Sulfates. The thermodynamic stability of the SO_4^{2-} group in sulfate polyanionic compounds $\text{Na}_2\text{M}(\text{SO}_4)_2 \cdot n\text{H}_2\text{O}$ ($M = \text{Fe, Mn, Co, Ni, etc.}$) is inferior, and its decomposition temperature is lower than 400°C . When exposed to temperatures above the decomposition temperature, SO_2 gas is easily released, resulting in low chemistry purity and toxic substances, so the low-temperature solid-phase method is often used for sulfate synthesis. According to the Pauling electromagnetic principle, the bonding of S–O is stronger than that of P–O, leading to the strong induction of sulfate. Thus, the energy level cleavage resulting from the hybridization of the d orbitals of transition metal ions with O 2p orbitals is intensified, making the redox potential of the material high. Since the charge-to-mass ratio of sulfate is significantly lower than that of phosphate, the theoretical specific capacity of sulfate materials is thus lower. Although in terms of practical applications, sulfate materials can hardly be comparable to commercialized LiCoO_2 , LiFePO_4 , NCM-811, and so on, they

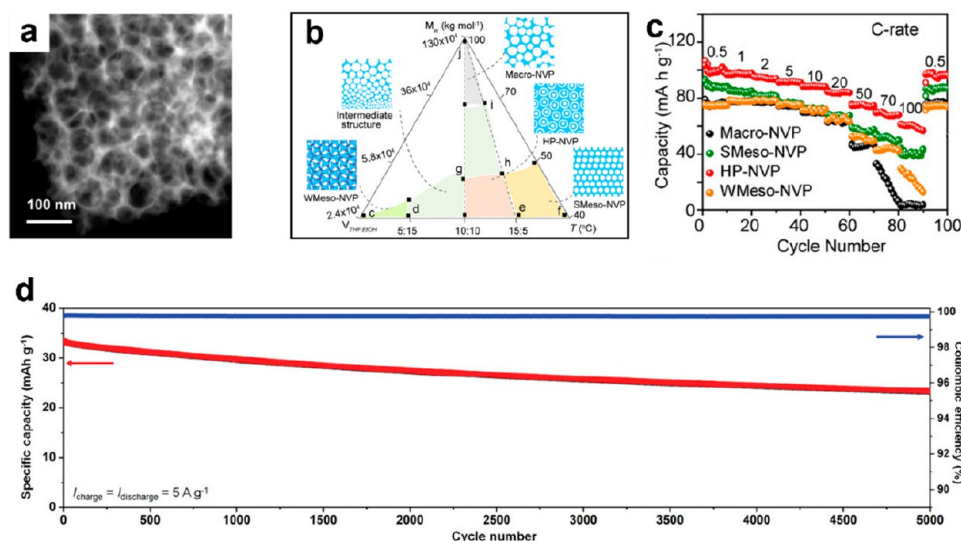


Figure 7. (a) TEM of the hierarchically porous $\text{Na}_3\text{V}_2(\text{PO}_4)_3$ materials and (b) ternary diagram of pore structure of porous NVP. (c) Rate capacities of the $\text{Na}_3\text{V}_2(\text{PO}_4)_3$ materials with different pore morphologies. Reproduced with permission from ref 91. Copyright 2021 Wiley-VCH. (d) Cycling performance of NVP@C@CNTs||NaPF6 in Diglyme||MCMC at 5 A g^{-1} . Reproduced with permission from ref 92. Copyright 2022 Wiley-VCH.

can unleash their own unique advantages in the field of low-cost energy storage. In 2014, Yamada et al. successfully prepared $\text{Na}_2\text{Fe}_2(\text{SO}_4)_3$, which belongs to monoclinic crystal system with the $P21/c$ space group.⁸⁰ It possesses a three-dimensional skeleton structure and Na^+ diffusion channels along the c -axis direction for Na^+ migration, delivering a theoretical capacity of 120 mA h g^{-1} with a high working platform of 3.8 V. As illustrated in Figure 6b, the FeO_6 octahedra form an isolated Fe_2O_{10} dimer by coedging and bridging with the SO_4 tetrahedra through the vertices, thus resulting in a three-dimensional (3D) skeletal structure with large ion channels along the c -axis. More specifically, Na^+ occupies three different Na sites in the 3D skeleton structure, where the Na2 and Na3 sites have 1D Na^+ diffusion channels along the c -axis and the Na^+ located at these two sites can easily diffuse along their respective channels.

3.1.3. Silicates. Silicates, represented as Na_2MSiO_4 ($M = \text{Fe, Mn, Co, Ni}$), are promising cathode candidates for large-scale energy storage because they possess the cost-effectiveness and resourcefulness of Na, Fe, and Si raw materials on Earth. Take $\text{Na}_2\text{FeSiO}_4$ as an example to dissect the structure of a silicate-based polyanionic compound. In monoclinic $\text{Na}_2\text{FeSiO}_4$ materials (space group Pn), the FeO_4 tetrahedron and SiO_4 tetrahedron are joined alternately to form a solid framework, while the sodium is hexacoordinated and forms a sublattice alone; Na ions are in a relatively disordered state in this structure (Figure 6c). Due to the large ion gap in the structure framework, Na^+ has greater freedom of motion, leading to a high Na^+ diffusion coefficient. Thus, high Na^+ diffusion in $\text{Na}_2\text{FeSiO}_4$ can still be achieved even without the fast ion transport channels, which also applies to Co-based and Mn-based silicate cathodes.⁸¹ $\text{Na}_2\text{FeSiO}_4$ with a high theoretical capacity of $\sim 278 \text{ mA h g}^{-1}$ corresponds to reversible insertion/extraction of two Na^+ per unit. Although theoretical studies showed the possibility of $2e^-$ reactions in silicate electrode materials, current studies show the occurrence of only the $1e^-$ reaction owing to electrolyte decomposition at potentials required to insert/extract the second Na^+ .⁸²

3.1.4. Borates. Reports on borate-based materials are much rarer. Borate polyanionic electrode materials have also received some attention from researchers because of their small molar mass, abundant resources, and environmental friendliness. Boron atoms can be sp^2 - and sp^3 -hybridized to form various groups, such as $[\text{BO}_3]^{3-}$, $[\text{BO}_4]^{5-}$, and $[\text{B}_2\text{O}_4]^{4-}$, that can be condensed or polycondensed to form islands, chains, layers and skeletal groups, leading to a variety of boronate crystal structures. Compared with other polyanionic compounds, borates have higher theoretical capacities but a much lower operating voltages due to the weak induction. The pentaborate polyanionic cathode material of $\text{Na}_3\text{MB}_5\text{O}_{10}$ (M stands for V, Fe, Mn, Co, etc.) can be easily fabricated by the solid-phase method. As illustrated in Figure 6d, $\text{Na}_3\text{FeB}_5\text{O}_{10}$ belonging to the orthogonal crystal structure (space group $Pbca$) consists of four vertices of FeO_4 tetrahedra connected to the $[\text{B}_5\text{O}_{10}]^{5-}$ unit, with the FeO_4 – B_5O_{10} network aggregated into layers in the ab -plane and stacked along the c -axis; Na^+ occupies the interlamination positions.⁸³ Additionally, its theoretical capacity is 78 mA h g^{-1} based on the reversible intercalation of one Na^+ per formula unit.

3.1.5. Mixed-Polyanion Materials. A series of hybrid polyanionic cathode materials with novel structures, such as a phosphate–pyrophosphate hybrid, a phosphate–carbonate hybrid, and fluorinated phosphate, can be obtained by taking advantage of their mutual compatibility. The phosphate–pyrophosphate hybrid polyanionic cathode material can be expressed as $\text{Na}_4\text{M}_3(\text{PO}_4)_2(\text{P}_2\text{O}_7)$ ($M = \text{Fe, Ni, Mn, Co, etc.}$). The crystal structure of $\text{Na}_4\text{M}_3(\text{PO}_4)_2(\text{P}_2\text{O}_7)$ is rhombohedral with a space group of $Pn21a$, according to Figure 6e, and the MO_6 octahedra and PO_4 tetrahedra form a double chain by covertex connections, which is further bridged to a laminar structure by P–O–P bonding of pyrophosphate.⁸⁴ The $\text{Na}_4\text{Fe}_3(\text{PO}_4)_2(\text{P}_2\text{O}_7)$ first reported by Kang's group exhibited excellent Na storage performance as a cathode for SIBs, with a high reversible specific capacity of 129 mA h g^{-1} with operating voltage of $\sim 3.2 \text{ V}$, achieving energy density of 412.8 Wh kg^{-1} .⁸⁹

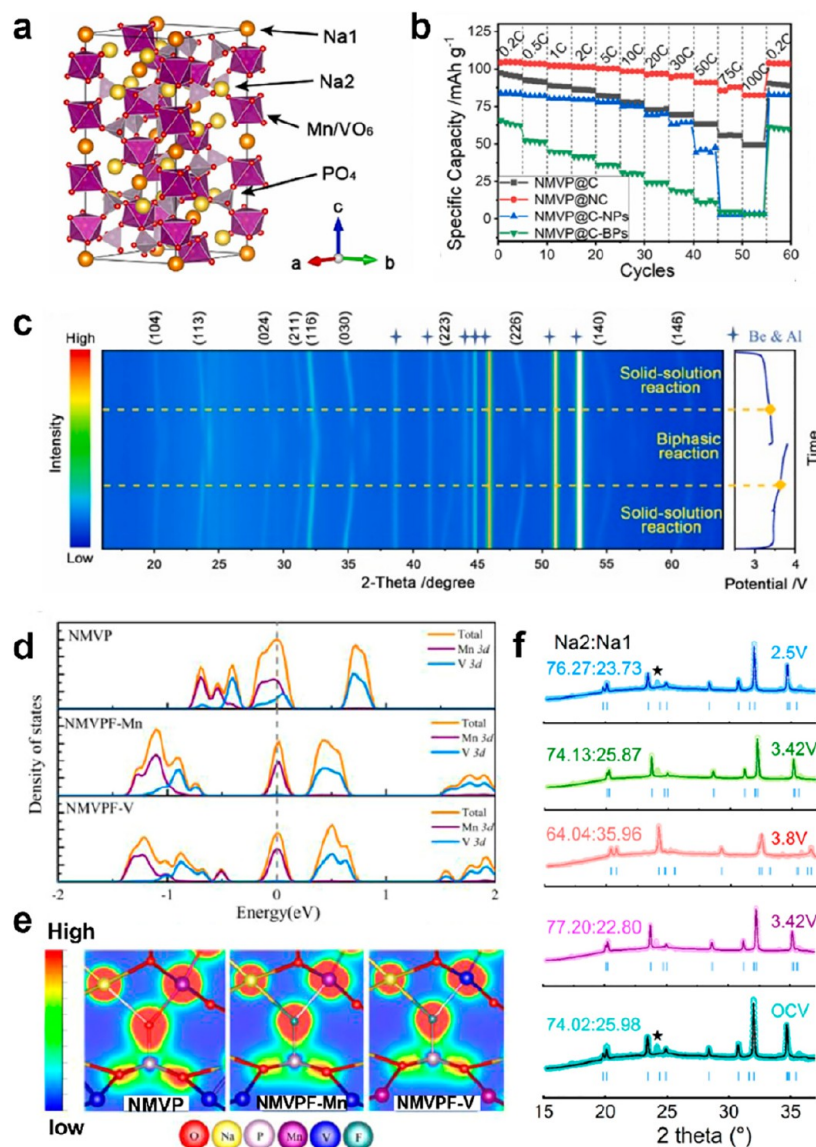


Figure 8. (a) Crystal structure of $\text{Na}_4\text{MnV}(\text{PO}_4)_3$, (b) rate performance of the NMVP-based cathode, and (c) in situ XRD pattern of $\text{Na}_4\text{MnV}(\text{PO}_4)_3$ @NC. Reproduced with permission from ref 96. Copyright 2022 Elsevier. (d) Total and projected density of states and (e) side-view of the electron density difference of NMVP and NMVPF-Mn/V samples. (f) Rietveld refinement of partial in situ XRD patterns of NMVPF. Reproduced with permission from ref 98. Copyright 2021 Elsevier.

In addition, a series of crucial fluorinated polyanionic materials with high voltages can be prepared by replacing part of the polyanion with high electronegativity fluorine, thereby developing NaVPO_4F , $\text{Na}_3\text{V}_2(\text{PO}_4)_2\text{F}_3$ (NVPF), $\text{Na}_3\text{V}_2(\text{PO}_4)_2\text{O}_2\text{F}$ (NVPOF), NaFeSO_4F , and other fluorinated materials. The tetragonal NVPF with a space group of $P4_2/mnm$ was composed of $[\text{V}_2\text{O}_8\text{F}_3]$ biotetrahedra and $[\text{PO}_4]$ tetrahedra that interconnected by angle sharing, and the occupancy ratio between Na(1) sites and Na(2) sites is 2:1. Owing to the high electronegativity of fluorine, the fluorinated material has a high working plateau of ~ 3.9 V with a theoretical capacity of ~ 130 mA h g^{-1} (corresponding to a theoretical energy density of ~ 500 W h kg^{-1}), thus being quite suitable for high-energy SIBs.^{85,86}

3.2. Promising Polyanionic Cathodes.

3.2.1. $\text{Na}_3\text{V}_2(\text{PO}_4)_3$. As one of the most widely studied polyanionic materials, $\text{Na}_3\text{V}_2(\text{PO}_4)_3$ (NVP) possesses high

ionic conductivity, excellent cycling stability and great thermal stability. Employed as the cathode for SIBs, $\text{Na}_3\text{V}_2(\text{PO}_4)_3$ has a theoretical capacity of 117.6 mA h g^{-1} and a working plateau of 3.4 V, which originated from the $\text{V}^{3+}/\text{V}^{4+}$ redox couple corresponding to two Na^+ ions involved in (de)sodiation.^{87,90} Unfortunately, the NVP cathode material characterized by sluggish diffusion kinetics and low electronic conductivity ($\sim 10^{-12}$ $\text{cm}^2 \text{ s}^{-1}$) has an unsatisfactory specific capacity and rate capability, and effective modifications are desired. At this stage, modification methods, including surface coating, morphological construction, and lattice modulation, have been developed. Recently, Xiong and coworkers proposed a polymer-stabilized droplet template strategy to synthesize a novel porous single-crystal-structured $\text{Na}_3\text{V}_2(\text{PO}_4)_3$ compound (Figure 7a), and selected area electron diffraction (SAED) confirmed its single-crystal structure. The phase diagram in Figure 7b summarizes the pore structures at the mesoscale and

macroscopic scales under various reaction conditions. When less volatile solvents combine with high-molecular-weight polyvinylpyrrolidone (PVP), hierarchically meso/macroporous structured NVP could be synthesized. Compared with the macroporous and mesoporous structures, the hierarchically porous structure with the 3D interlinked channel provides faster Na^+ transport paths and a larger contact area, effectively accelerating the Na^+ transportation. Another advantage is that Na^+ can migrate along the smooth solid–liquid interface in the HP-NVP. As a consequence, an outstanding rate capability of 61 mA h g^{-1} at ultrahigh rate of 100 C and a prolonged lifespan of 10000 cycles at 20 C without capacity fading can be achieved (Figure 7c). Specially, HP-NVP was assembled to form a symmetric cell, which exhibits a specific capacity of 47 mA h g^{-1} at 50 C and stable cycling at 10 C for 700 cycles.⁹¹ Xu et al. proposed a spray drying method for synthesizing NVP/rGO HSs. Owing to the unique porous hollow architecture effectively shortening the Na^+/e^- diffusion path, the synthesized NVP/rGO HSs compound manifested a high reversible capacity of 116 mA h g^{-1} at 1 C (98% of theoretical capacity), an outstanding high-rate capability of 98.5 mA h g^{-1} at 20 C, as well as a stable cycling performance of 73.1 mA h g^{-1} over 1000 cycles at 10 C. To explore the practical application of NVP/rGO HSs cathode, the full cells assembled with NVP-HSs cathode and S-CMTs anode exhibit a capacity retention of 84.2 mA h g^{-1} after 100 cycles at 1 C. Assembling a high-performance sodium-ion full battery (SIFB) requires overall matching between the cathode, anode and electrolyte. Wei et al. proposed an excellent SIFB integrated with an optimized NVP@C@carbon nanotube (NVP@C@CNTs) cathode, a mesocarbon microbead (MCMB) anode, and a Na^+ –diglyme electrolyte. The as-synthesized NVP@C@CNT cathode displays a high electronic conductivity, reducing the overpotential and charge transfer resistance and leading to a superior rate capability at a high rate of 80 A g^{-1} . Besides, it demonstrated a discharge capacity of 70 mA h g^{-1} with extraordinary stability over ultralong 20 000 cycles at a high current density of 20 A g^{-1} . Furthermore, the NVP@C@CNTs/MCMB full cell obtained high energy density of 88 W h kg^{-1} at $\sim 10 \text{ kW kg}^{-1}$ and 58 W h kg^{-1} at $\sim 23 \text{ kW kg}^{-1}$. Besides, superior cyclability with 72.7% capacity retention for 5000 cycles at 5 A g^{-1} could be achieved (Figure 7d). Both the high conductivity of NVP@C@CNT cathode and the expanded ion diffusion paths at the anode resulted from the initial pseudocapacitive intercalation, which contributed to this high rate capability and excellent cyclability.⁹²

In addition to morphological construction and surface coating, lattice regulation is also beneficial for improving NVP performance. Most studies primarily concentrate on introducing inactive elements into the V site. Liang et al. fabricated Mo-doped 1D NVP nanowires (MNVP@C NWs) as a multifunctional cathode for Na storage and fully explored their practicality.⁹³ The electron energy loss spectroscopy (EELS) confirmed the uniform distribution of external Mo within the nanowires rather than surface doping. This cathode obtained a discharge capacity of 116.8 mAh g^{-1} at 0.1 C and displayed a capacity retention of 85.7% after 8000 cycles at 5 C. Additionally, the constructed pocket-flexible SIBs demonstrated a large energy density of $262.4 \text{ W h kg}^{-1}$ and an ultrahigh rate capability of 77 mA h g^{-1} at 150 C. This is because when higher valence Mo^{6+} was introduced into the NVP, Na^+ vacancies would be generated due to valence equilibrium, which enhanced the electronic conductivity and

ion diffusion kinetics of the electrode due to the smaller Na^+ migration barrier. Besides, Shi et al. developed a cathode of bismuth-doped NVP wrapped with carbon nanotubes.⁹⁴ The optimized $\text{Na}_3\text{V}_{1.97}\text{Bi}_{0.03}(\text{PO}_4)_3/\text{C}@\text{CNTs}$ sample displayed a reversible capacity of 97.8 mA h g^{-1} and maintained a capacity of 80.6 mA h g^{-1} over a prolonged 9000 cycles at 12 C. Even when cycled at an ultrahigh rate of 80 C, the cathode also exhibited a high capacity of 84.3 mA h g^{-1} and achieved 87% of its capacity after 6000 cycles. These excellent rate capability and outstanding cyclability can be attributed to the doped Bi^{3+} that acted as the pillar of NVP crystal structure, buffering crystal deformation and enhancing the structural stability.

3.2.2. $\text{Na}_3\text{VM}(\text{PO}_4)_3$. Vanadium-based materials profiting from multivalence states and rich resource of vanadium are some of the preferred electrodes for batteries, but vanadium has high toxicity. Thus, cost-efficient and environment-friendly elements (e.g., Fe, Mn) are doped into the V-site in $\text{Na}_3\text{V}_2(\text{PO}_4)_3$, producing $\text{Na}_4\text{VFe}(\text{PO}_4)_3$ and $\text{Na}_4\text{VMn}(\text{PO}_4)_3$. As illustrated in Figure 8a, $\text{Na}_4\text{VMn}(\text{PO}_4)_3$ is constructed by MnO_6/VO_6 octahedra sharing all the corners with PO_4 tetrahedra, and it possesses a theoretical capacity of 111 mA h g^{-1} and voltage plateaus of 3.6 ($\text{Mn}^{2+}/\text{Mn}^{3+}$) and 3.3 V ($\text{V}^{3+}/\text{V}^{4+}$) corresponding to reversible insertion/extraction of two Na^+ . Except for suffering from low electron migration kinetics, the Jahn–Teller effect of Mn^{3+} will lead to Mn digestion and structural instability, shortening the lifespan of the $\text{Na}_3\text{VM}(\text{PO}_4)_3$ electrode.⁹⁵ The most facile and effective way to improve the electronic conductivity of $\text{Na}_3\text{VM}(\text{PO}_4)_3$ is to coat it with conductive materials. Recently, Zhu et al. designed a unique hierarchical bayberry-like NMVP@NC material as a cathode for SIBs via facile ball-milling and subsequent calcination. Even cycled at an ultrahigh rate of 100 C, the NMVP@NC cathode can still deliver a high discharge capacity of 82.4 mA h g^{-1} (Figure 8b), which is far superior to other NMVP-based electrodes. When assembled with commercial soft carbon as the anode, the full cell could deliver 94 mA h g^{-1} at 0.1 C and 57 mA h g^{-1} at 10 C. Figure 8c reveals the structural evolution of the NMVP@NC cathode during the first electrochemical cycle. The NMVP@NC cathode underwent a solid-solution reaction when charged to 3.6 V and a biphasic reaction in the interval of 3.6–3.8 V. Besides, peaks during the discharge and the charge process appear symmetric, confirming the high reversibility of the electrochemical reactions. The NMVP@NC cathode is unique: (i) the ultrasmall sizes of nanoparticles render a short diffusion distance for Na^+ and provide a larger electrode/electrolyte contact area, (ii) the 3D N-doped carbon network available improves the electrical conductivity of NMVP, and (iii) the robust structure suppresses the volumetric expansion during the repeated Na^+ insertion/extraction, giving rise to superior cyclability.⁹⁶

To mitigate the malignant effects caused by Mn^{3+} , more modification of $\text{Na}_4\text{MnV}(\text{PO}_4)_3$ associated with heteroatomic doping of Al^{3+} , Mg^{2+} , and other elements has been explored. The substitution by heteroatoms is aimed at reducing the concentration of Mn^{3+} in the NVMP cathode so that the Jahn–Teller distortion is suppressed and structural stability is enhanced with increased covalency by inducing shorter (V/Mn/Mg/Al)–O bond lengths. Moreover, the substitution of inert Al^{3+} into the NVMP structure would generate abundant Na vacancies, which are expected to reduce the activation energy and enhance the Na^+ mobility.⁹⁷ In addition to doping at the vanadium sites, doping at the polyanion sites has also

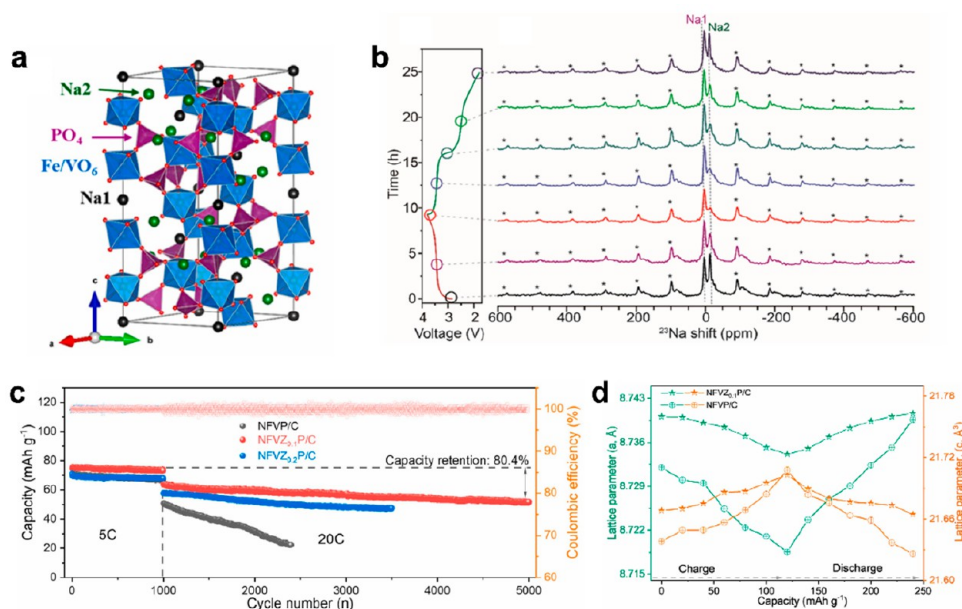


Figure 9. (a) Crystal structure of $\text{Na}_4\text{FeV}(\text{PO}_4)_3$. (b) ^{23}Na magic-angle-spinning (MAS) NMR of NFVP@C at different cycle states. Reproduced with permission from ref 99. Copyright 2022 Elsevier. (c) Cycling performance of NFVP/C with varying Zr-content (0–0.2). (d) Variation of the lattice parameters of NFVP/C and NFVZ_{0.1}P/C electrodes. Reproduced with permission from ref 101. Copyright 2022 Elsevier.

been studied. The innovative Na-deficient $\text{Na}_{3.85}\square_{0.15}\text{MnV}(\text{PO}_{3.95}\text{F}_{0.05})_3$ material was fabricated by partially doping F into the NMVP. Electron density differences shown in Figure 8d and e prove that the change of electron density caused by the substituted F near Mn or V atoms and the weak Coulomb interaction induced by the Na vacancy effectively promotes the Na^+ diffusion dynamics. Executing *ex situ* ^{23}Na NMR and *in situ* XRD (Figure 8f) characterization of NMVPF electrodes at different states of (dis)charge revealed the higher Na^+ extraction rate from the Na2 site.⁹⁸

$\text{Na}_4\text{FeV}(\text{PO}_4)_3$ belonging to the $\text{Na}_4\text{VM}(\text{PO}_4)_3$ type is another promising cathode for SIBs with a similar framework as $\text{Na}_4\text{MnV}(\text{PO}_4)_3$. It is constructed by FeO_6/VO_6 octahedra with PO_4 tetrahedra (Figure 9a). Lu et al. proposed a novel $\text{Na}_4\text{FeV}(\text{PO}_4)_3$ @C cathode synthesized via a combined ball-milling, sol-gel, and calcination process. The as-prepared $\text{Na}_4\text{FeV}(\text{PO}_4)_3$ @C exhibited specific capacities of 100 mA h g^{-1} at 0.1 C and 80.6 mA h g^{-1} at 10 C when tested at the wide voltage window of 1.3–3.8 V. In charge–discharge curves, two plateaus located at 2.5 and 3.5 V can be ascribed to $\text{Fe}^{2+}/\text{Fe}^{3+}$ and $\text{V}^{3+}/\text{V}^{4+}$ redox couples, respectively. Besides, the cathode exhibited great cycling stability, with 96.8% capacity retention after 800 cycles at 5 C, surpassing the original $\text{Na}_4\text{FeV}(\text{PO}_4)_3$ cathode that rapidly decays after only 400 cycles. The solid-state ^{23}Na nuclear magnetic resonance revealed that the Na^+ stand at Na2 sites exhibited faster insertion/extraction dynamics upon cycling (Figure 9b). XRD and time-of-flight neutron powder diffraction illustrated that the electrochemical process undergoes a reversible solid-solution reaction, confirming its stable framework structure.⁹⁹ Wang et al. reported a bicarbon-decorated NFVP@rGO@CNT material as the cathode for SIBs. A high discharge capacity of 156 mA h g^{-1} at 0.1 C could be achieved in the operating window of 2.0–4.4 V. Besides, a rate capacity of 60 mA h g^{-1} at 30 C and 71% capacity retention over 600 cycles at 2 C were realized. Such great rate performance and cyclability benefit from the double carbon layer (CNTs and rGO) accelerating the

electron transfer. Even when fabricated with a high mass loading of 6.2 mg cm^{-2} , the cathode exhibited excellent rate capability and cyclability (58.7 mA h g^{-1} at 30 C and 72.1% capacity retention after 1000 cycles at 10 C), confirming its practical potential.¹⁰⁰ Ma et al. reported a heteroatomic doping strategy in $\text{Na}_4\text{FeV}(\text{PO}_4)_3$ materials, which generate extra Na vacancies to boost the electroconductivity. The optimized $\text{Na}_{3.9}\text{FeV}_{0.9}\text{Zr}_{0.1}(\text{PO}_4)_3/\text{C}$ electrode exhibited a high discharge capacity (114 mA h g^{-1} at 0.1 C), superior rate capability (66.7 mA h g^{-1} at 0.1 C), and remarkable cyclability of 82.4% capacity retention over 4000 cycles at 20 C (Figure 9c). As illustrated in Figure 9d, the NFVZ_{0.1}P/C cathode showed a smaller volume change ($\Delta V/V_{\text{pristine}}$) of $\sim 5.21\%$ during electrochemical cycling compared with the undoped sample. Its excellent structural stability benefited from the pillar support from Zr. Furthermore, the assembled NFVZ_{0.1}P/C||HC full cell exhibited a superior rate capacity of 56.4 mA h g^{-1} at 1000 mA g^{-1} and 97% capacity retention over 100 cycles at 200 mA g^{-1} .¹⁰¹

More recently, a high-entropy crystal substitution strategy for promoting polyanionic materials was proposed by Li and coworker, and $\text{Na}_3\text{VAl}_{0.2}\text{Cr}_{0.2}\text{Fe}_{0.2}\text{In}_{0.2}\text{Ga}_{0.2}(\text{PO}_4)_3$ (denoted as NVMP) was developed via a facile sol-gel method and explored for SIBs at both ambient and low temperatures. Benefiting from the doping of high-entropy crystals, the activity of $\text{V}^{4+}/\text{V}^{5+}$ electron couples is activated, enabling a highly reversible capacity of 102 mA h g^{-1} at 0.1 C. Besides, the NMVP half-cell also showed outstanding cyclability over 5000 cycles at 20 C. Even tested at -20°C , the NVMP cathode could still demonstrate prolonged cyclability with 94.2% capacity retention over 1000 cycles at a high rate of 5 C. For a real application, the constructed NVMP||HC full batteries could deliver 81 mA h g^{-1} at 0.2 C and steadily cycle for 50 cycles when paired with hard carbon.¹⁰²

The element doping strategy for polyanionic compounds, particularly vanadium-based phosphates, focuses on using more cost-effective transition metal elements (e.g., Mn, Fe,

etc.) to replace V, achieving a lower vanadium content while maintaining similar electrochemical performance. Mn substitution brings about higher voltage plateaus (3.6 V), but it also generates an unfavorable Jahn–Teller effect. To address this, additional atoms such as nonactive metal elements like Al, Mg, Ce, and Cr are introduced to suppress the adverse effects caused by Mn^{3+} .¹⁰³ The introduction of Fe stabilizes the lattice further, but the overall decreased voltage (~ 3.0 V) limits its application in high-energy-density SIBs, making it less favorable. On the other hand, the introduction of highly electronegative fluorine at polyanion sites has proven to be an effective strategy for promoting the working voltage of polyanionic compounds. However, it is crucial to note that excessive F content hinders the transmission of Na^+ in the lattice, necessitating strict control over its introduction amount. Furthermore, utilizing high-entropy crystal substitute and activating electron redox with higher valence states are promising avenues for future research.

3.3. Scalable Preparation of Polyanionic Compounds.

The scalable preparation of polyanionic materials is also of great concern. Qi et al. proposed a groundbreaking synthesis route for the scalable production (150 g per batch) of multishelled $\text{Na}_3(\text{VOPO}_4)_2\text{F}$ microspheres using in situ generated bubbles as soft templates at room temperature.¹⁰⁴ In this method, raw materials were extracted from vanadium slag and NVPOF microspheres were formed during the coprecipitation process with the appropriate reaction time. The large-scale prepared $\text{Na}_3(\text{VOPO}_4)_2\text{F}$ exhibited an outstanding rate capacity of 81 mA h g^{-1} and remarkable cycling stability, with 70% capacity remaining over 3000 cycles at 15 C. This room-temperature scalable production strategy paves the way for the commercialization of SIBs. Similarly, Shen and coworker developed a rapid synthesis route for $\text{Na}_3\text{V}_2(\text{PO}_4)_2\text{O}_2\text{F}$ using a solvent-free room-temperature solid-phase mechanochemical method, and they rigorously verified the feasibility of production using ten different types of vanadium raw materials.¹⁰⁵ The optimized NVPOF@8%KB demonstrated a high initial capacity ($142.2 \text{ mA h g}^{-1}$ at 0.1 C), superior rate capability ($112.8 \text{ mA h g}^{-1}$ at 20 C), and remarkable cyclability (maintaining 98% capacity over 10 000 cycles at 20 C). To confirm the feasibility of large-scale production of sodium vanadium fluorophosphate using mechanochemical methods, a kilogram-scale preparation was executed. Subsequently, the large-scale synthesized NVPOF materials were matched with a hard carbon anode to fabricate a 26650 cylindrical battery, which delivered a high capacity of 1500 mA h g^{-1} and an energy density of $\sim 90 \text{ Wh kg}^{-1}$. The successful kilogram-scale production and the excellent electrochemical performance of the large-scale synthesized product further validate the feasibility of the mechanochemical method for the commercial SIB cathode materials.

4. PRUSSIAN BLUE CATHODES

Hexacyanoferrates (HCFs)/Prussian blue (PB) and its analogues (PBAs) are promising cathode candidates for SIBs owing to their low cost, easy preparation, and open framework structure for Na^+ accommodation.^{6,106,107} The chemical formulas of PBAs could be denoted as $\text{Na}_x\text{M}_1[\text{M}_2(\text{CN})_6]_y\text{zH}_2\text{O}$ ($0 \leq x \leq 2$, $0 \leq y \leq 1$), where $\text{M}_1 = \text{Fe, Mn, Ni, Cu, Co, Zn, etc.}$; $\text{M}_2 = \text{Fe, Mn, Co}$; and \square represents a transition metal coordinated with N and C atoms and $[\text{M}_2(\text{CN})_6]$ vacancies inside the crystal structure, respectively.¹⁰⁸ The crystal structures of PBAs can be cubic,

monoclinic, rhombohedral, and trigonal, which vary according to the number of Na^+ ions and the content of water. Generally, the alkaline-deficient PBAs present a cubic structure, while alkaline-rich PBAs show a monoclinic phase.¹⁰⁹ After dehydration treatment, the phase structure will be transformed to rhombohedral or trigonal for the reduced amount of water.¹¹⁰ The specific capacities of PBAs depend on chemical compositions when applied as cathode materials for SIBs (e.g., 85 mA h g^{-1} for a single-electron redox-active site (SE-PBAs $\text{M}_1 = \text{Zn, Ni}$) and 170 mA h g^{-1} for double-electron redox-active sites (DE-PBAs, $\text{M}_1 = \text{Mn, Fe, Co}$)). Taking into account the high average discharging voltage (above 3.0 V vs Na^+/Na), the theoretical energy density of DE-PBAs could reach 510 Wh kg^{-1} , which is competitive with commercial LiFePO_4 employed in LIBs.¹¹¹

Typically, PBAs are prepared by simple coprecipitation of sodium hexacyanoferrate and transition metal salts in water. However, the obtained PBAs present a random distribution of H_2O and $[\text{M}_2(\text{CN})_6]$ vacancies because of the rapid reaction between the hexacyanoferrate ligand and transition metal ions.¹² Additionally, the H_2O in PBAs can be divided into three species: (i) H_2O adsorbed on the surface, (ii) interstitial or zeolite H_2O located at the alkali metal ion sites, and (iii) coordinated H_2O chemically bonded with transition metals for the absence of $[\text{M}_2(\text{CN})_6]$. The $\text{H}_2\text{O}/\text{vacancies}$ in PBAs would cause lattice distortion and even structure collapse during (de)sodiation processes, leading to rapid capacity degradation.¹¹² Meanwhile, the irreversible phase transition during charging and discharging process also contributes to the short cycle lifespan. Further, low electronic conductivity for poor rate performance of PBAs is another obstacle should be overcome for practical application.¹¹³ As a consequence, strategies aiming at preparing PBAs with low levels of water and vacancies, mitigated phase transitions during cycling, and enhanced electronic conductivity are imperative and challenging.

4.1. Modification of Prussian Blue Materials. Although many metals are capable of occupying the M_1 and M_2 sites, the Fe-based ($\text{M}_1 = \text{M}_2 = \text{Fe}$) and Mn-based ($\text{M}_1 = \text{Mn, M}_2 = \text{Fe}$) PBAs with two redox-active centers are the most investigated for their high theoretical specific capacity and low cost. Besides of the high content of $\text{H}_2\text{O}/[\text{Fe}(\text{CN})_6]$ vacancies and low electronic conductivity, Fe-based PBAs also suffer from a low practical specific capacity for the irreversible electrochemical reaction of low-spin Fe coordinated with C,¹¹⁴ and the Mn-based PBAs suffer from the Jahn–Teller effect of Mn^{3+} and the dissolution of Mn^{2+} .^{115,116} Crystal structure control, non-aqueous preparation/dehydration treatment, compositing with conductive carbon, surface coating, and cationic doping are effective approaches to prepare PBAs with low $\text{H}_2\text{O}/\text{vacancy}$ contents, high crystallinity, high electronic conductivity, and improved the electrochemical performance according to the previous studies, which are summarized in this section. In addition, the scalable preparation of PBAs and its practical application in full-cells were also introduced.

4.1.1. Crystal Structure Control. $[\text{Fe}(\text{CN})_6]$ vacancies inside the PBA crystal were generated during the fast coprecipitation between metal salts and sodium hexacyanoferrate. The vacancies occupied by coordinated water and interstitial water reduce the amount of extractable sodium, hinder the migration of Na^+ , and decrease the practical specific capacity.^{117,118} Additionally, the crystal structure of defect-rich PBAs tends to collapse during (de)insertion of Na^+ due to the

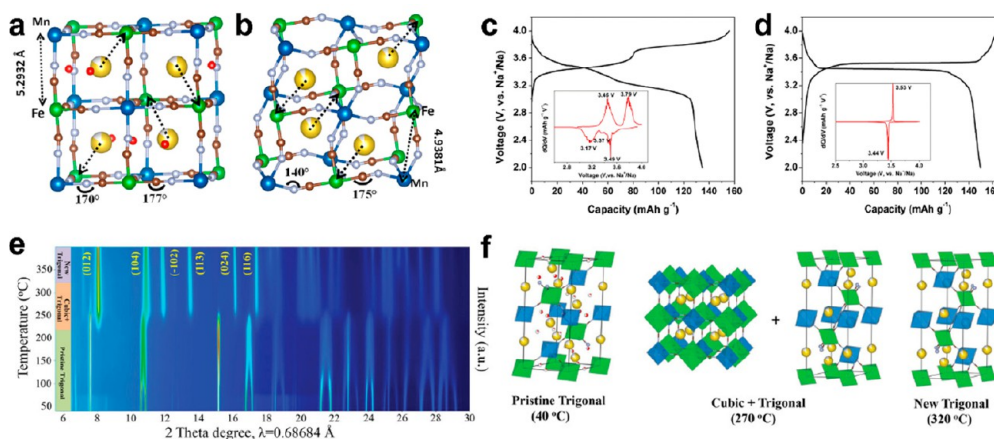


Figure 10. Local structures of (a) M- $\text{Na}_{2-\delta}\text{MnHCF}$ and (b) R- $\text{Na}_{2-\delta}\text{MnHCF}$ and galvanostatic initial charge and discharge profiles of (c) M- $\text{Na}_{2-\delta}\text{MnHCF}$ and (d) R- $\text{Na}_{2-\delta}\text{MnHCF}$. Reproduced with permission from ref 110. Copyright 2015 ACS publications. (e) 2D contour map of in situ high-temperature synchrotron X-ray diffraction patterns of as-prepared $\text{Na}_{2-x}\text{FeFe}(\text{CN})_6$ samples under Ar and (f) corresponding crystal structures at 40, 270, and 320 °C. Reproduced with permission from ref 112. Copyright 2022 Wiley-VCH.

absence of bulky $[\text{Fe}(\text{CN})_6]$, which deteriorates the electrochemical performance.¹⁵ It is documented that the critical point for decreasing the $[\text{Fe}(\text{CN})_6]$ vacancies and enhancing the crystallization of PBAs is slowing down the reaction rate of coprecipitation. Pioneer researchers have put forward several effective strategies to reduce the rate of coprecipitation: (i) Implementing chelating agent/surfactant-assisted precipitation. A chelating agent, such as sodium citrates (Na_3Cit),¹¹⁹ ethylenediaminetetraacetic acid disodium (Na_2EDTA),¹²⁰ diethylenetriaminepentaacetic acid disodium (Na_2DTPA),¹²¹ and pyrophosphoric salts ($\text{Na}_4\text{P}_2\text{O}_7$)^{122,123} having high complexation with transition metal salts could slow down the release rate of metal ions and the crystallization ratio. (ii) Lowering the precipitation temperature for Fe-based PBAs. Our group¹²⁴ found that Fe-based PBAs prepared below 0 °C or iced conditions exhibited fewer $[\text{Fe}(\text{CN})_6]$ vacancies than those synthesized at room or high temperature for the decreased reaction rate, which was consistent with the result of Ma's group.¹²⁵ (iii) Preparing a high salt concentration. Guo's group reported Mn-PBAs fabricated using a saturated $\text{Na}_4\text{Fe}(\text{CN})_6$ solution displayed only 4% vacancies (24% at traditional condition), and vacancy-free Mn-PBAs could be obtained once the sample was aged at 80 °C for 20 h.¹²⁶

4.1.2. Nonaqueous Preparation/Dehydration Treatment. Although several reports demonstrated that the interstitial water located at body-centered sites can stably exist in PBAs for structural stabilization,¹²⁷ most researchers believed that the deteriorated electrochemical properties of PBAs are due to the side reactions between water and the nonaqueous electrolyte.¹²⁸ It was found in our group that the water content of the PBA cathode at the discharging state could reach the ultrahigh value about 20 ppm, which was fivefold higher than those in $\text{Na}_3\text{V}_2(\text{PO}_4)_3$, and resulted in the swell of pouch cell.¹¹² Therefore, it is imperative to solve the water problem of PBAs to promote their commercial application. Normally, preparing PBAs in a nonaqueous solution and performing a dehydration treatment after primary drying are effective methods to reduce the water content.

4.1.2.1. Nonaqueous Preparation. As we discussed above, PBAs were prepared in an aqueous solution, making it difficult to completely eliminate the crystal water (10–15 wt %). Substitution of partial/whole water by organic solvents has

been proven effective to suppress crystal water growth in PBAs. You's group demonstrated that high-crystallinity PBAs with a low water content (7.90%) could be synthesized by the solvothermal method using an ethylene glycol/water mixed solvent to minimize water content in the reaction environment and decrease the crystal nucleation rate.¹²⁹ However, water in the reaction was necessary to dissolve $\text{Na}_4\text{Fe}(\text{CN})_6$ precursors. To improve the solubility of the precursor and accelerate the reactions in organic solutions, He's group developed a microwave-assisted solvothermal approach with anhydrous ethanol as the solvent. The microwave supplies external energy, and PBAs could be synthesized at a slightly elevated temperature within hours.¹³⁰ As a result, the content of interstitial water in obtained samples is only 4.34–5.13 wt %, and a high discharging specific capacity of 150 mA h g^{-1} could be reached, suggesting organic solvents are alternative mediums for the preparation of PBAs. Recently, our group proposed a “water-in-salt” nanoreactor strategy to prepare highly crystallized Mn-based PBAs with a decreased water content (10.1% vs 18.5% prepared by coprecipitation), higher volume yield, and enhanced electrochemical performance over a wide temperature range from –10 to 50 °C, indicating it was a promising route to achieve the large-scale production of PBAs.¹³¹

4.1.2.2. Dehydration Treatment. Goodenough's group first proposed the post-dehydration of Mn-based PBAs at low temperature (100 °C) heating under high-vacuum (15 mTorr) for the removal of interstitial water.¹¹⁰ After the dehydration treatment, the water content in $\text{Na}_{2-\delta}\text{MnHCF}$ decreased from 12% to 2%, indicating the z value was only 0.3 in dehydrated $\text{Na}_{2-\delta}\text{MnHCF}$. Meanwhile, the monoclinic $\text{Na}_{2-\delta}\text{MnHCF}$ (M- $\text{Na}_{2-\delta}\text{MnHCF}$) converted to the rhombohedral phase (R- $\text{Na}_{2-\delta}\text{MnHCF}$) after the dehydration treatment due to lattice shrinking and distortion, as shown in Figure 10a and b. The electrochemical behavior was also changed after the removal of interstitial water. The M- $\text{Na}_{2-\delta}\text{MnHCF}$ electrode show two pairs redox peaks located at 3.17/3.45 and 3.49/3.79 V, and a discharging capacity of 137 mA h g^{-1} could be delivered (Figure 10c), while R- $\text{Na}_{2-\delta}\text{MnHCF}$ displayed an apparently single flat plateau at 3.44/3.53 V and a higher initial discharging capacity of 150 mA h g^{-1} (Figure 10d). Additionally, the dehydrated $\text{Na}_{2-\delta}\text{MnHCF}$ exhibited promis-

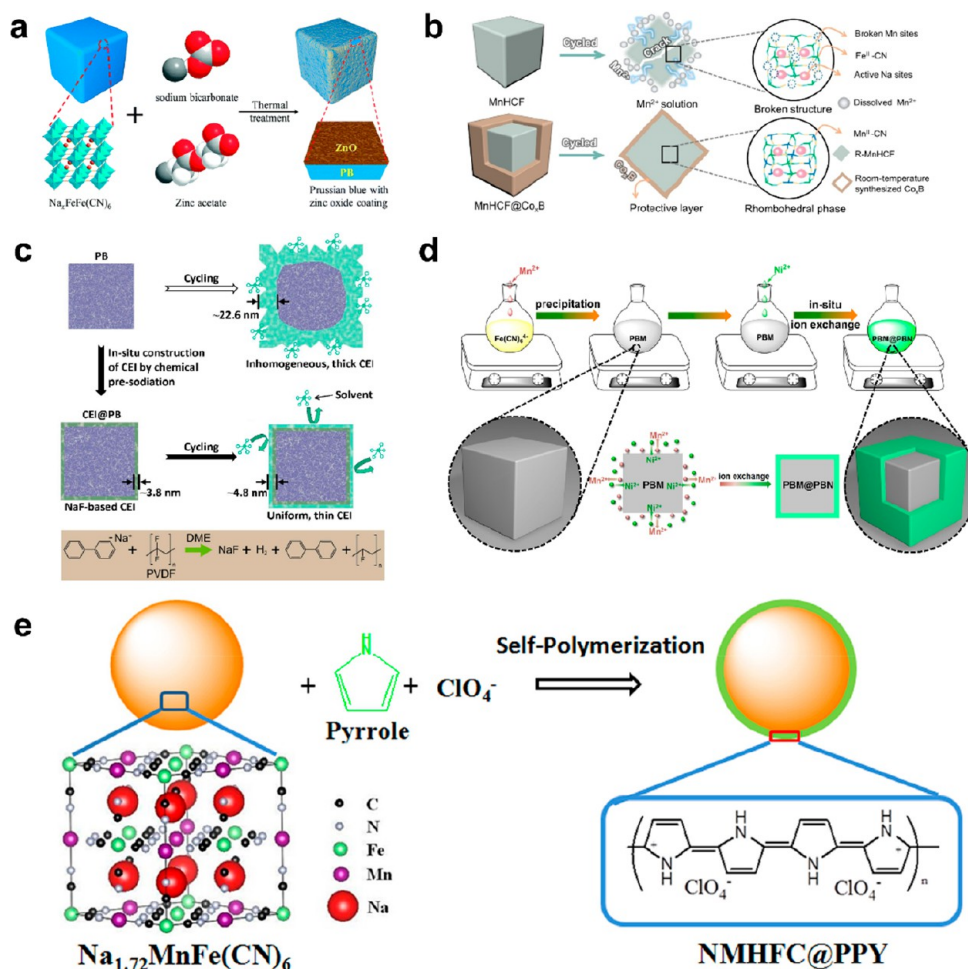


Figure 11. Coating layers for PBAs: (a) ZnO (reproduced from ref 137, copyright 2019 Royal Society of Chemistry), (b) Co_xB (reproduced from ref 138, copyright 2023 Wiley-VCH), (c) artificial NaF-rich CEI (reproduced from ref 139, copyright 2022 Elsevier), (d) Ni-HCF (reproduced from ref 115, copyright 2021 Elsevier), and (e) PPY (reproduced from ref 140, copyright 2015 Elsevier).

ing cycling performance (75% capacity retention after 500 cycles) and rate capability (81% capacity retention at 20 °C). A similar conclusion has been drawn by Younesi's group, that is, the phase structure of Fe-PBAs converted from monoclinic to rhombohedral after dehydration.¹³² Furthermore, the relationship between the water content and phase structure of sodium-rich Na_{2-x}FeFe(CN)₆ was systematically studied in our group.¹¹² As depicted in Figure 10e and f, the pristine trigonal phase was maintained when adsorbed water was removed (<150 °C), while cubic and new high-temperature trigonal phases could be found from 220 to 300 °C; the trigonal phase dominated at 270 °C, at which the interstitial and coordinated water faded away. The cubic phase disappeared at temperatures higher than 300 °C, and the new trigonal phase was stable up to 400 °C. After dehydration at 270 °C under Ar, the low-spin Fe²⁺/Fe³⁺ redox reaction at ≈3.4 V was activated and the specific capacities were improved. Moreover, the dehydrated Na_{2-x}FeFe(CN)₆ exhibited excellent cycling performance (98.9% capacity retention after 2000 cycles at 100 mA g⁻¹), evidencing that post-dehydration was an effective strategy to reduce the water content and improve the electrochemical performance of PBAs.

4.1.3. Compositing with Conductive Carbon. Although the 3D open framework inside the PBAs facilitated Na⁺ diffusion, the rate capability of PBAs is below expectation for their

limited electronic conductivity. Compositing PBAs with conductive carbon has been considered as an effective strategy to improve their rate performance. Hence, considerable research has been devoted to building mesoscopic or nanoscopic interactions between conductive carbon (carbon nanotubes (CNT),¹¹³ Ketjen black (KB),¹³³ graphene,¹³⁴ ordered mesoporous carbon (CMK-3),¹³⁵ and 3D N-doped ultrathin carbon (3DNC),¹³⁶ among others, and PBAs particles by in situ growth or chemical coprecipitation. Goodenough's group constructed monodispersed PBAs nanocubes nucleating on a CNT conductive network (PB/CNT).¹¹³ The "built-in" CNT network accelerated the electron transport and thus the sodiation reaction of PBAs. As a result, PB/CNT delivered a high discharge capacity of 142 mA h g⁻¹ at 0.1 C under subzero temperatures (-25 °C), corresponding to 85% capacity retention compared with that at 25 °C. A reversible capacity of 52 mA h g⁻¹ at 6 C could be obtained at -25 °C, while it is only 2 mA h g⁻¹ for bare PBAs. After that, Dou and coworkers synthesized a PB@C composition through a facile and in situ solution method, with NaFeHCF directly grown on KB chains.¹³³ Despite the degraded electrochemical activity of Fe^{LS}(C) caused by [Fe(CN)₆]⁻ vacancies, the perfectly shaped PB@C composition with a lower vacancy content (7% vs 15% for bare PB) and fast charge/Na⁺ diffusion exhibited a higher reversible capacity

(130 mA h g⁻¹ vs 90 mA h g⁻¹ at 0.5 C, 1C = 100 mA g⁻¹) and unprecedented rate capacity (77.5 mA h g⁻¹ at 90 C). Owing to the large specific surface and superior electrical conductivity, 3DNC networks were considered as an ideal skeleton for loading redox-active materials. Zhao's group found that the Na⁺ adsorption energy at interfaces was decreased and Fe 3d charges were more delocalized after the introduction of 3DNC (8.26 wt %) into NaK-MnHCF, contributing to the better rate performance of the NaK-MnHCF@3DNC composite compared to the bare NaK-MnHCF. Therefore, compositing affords a simple solution to resolve the low electrical conductivity for PBAs.¹³⁶

4.1.4. Surface Coating. It is well acknowledged that PBA cathodes suffer from serious capacity fading due to the transition metal dissolution and side reactions between the electrode materials and organic electrolytes. Thus, surface coating has been used to protect the PBAs from metal dissolution and unwanted side reactions. Considering the instability of PBAs at temperatures higher than 350 °C, however, only low-temperature surface coating is suitable for PBAs. Up to now, inorganic materials, stable SE-PBAs materials (Ni-HCF), and conductive carbon/polymers have been applied as protective layers for electrochemical performance enhancement, as illustrated in Figure 11.

4.1.4.1. Inorganic Materials. Liu's group constructed a semiconducting and chemically stable ZnO layer (~50 nm) on the surface of Na_xFeFe(CN)₆ (PB@ZnO) via a thermal treatment at 200 °C under N₂ (Figure 11a), which helped reduce the charge-transfer resistance and prohibit the decomposition of the PB lattice.¹³⁷ In order to suppress the microstructural degradation and undesirable Jahn–Teller effect, Hu's group recently created a magical Co_xB on the MnHCF surface through a facile wet-chemical coating method (Figure 11b).¹³⁸ Owing to the whole coverage of Co_xB, the optimal MnHCF-5%Co_xB cathode displayed limited Mn dissolution and reduced intergranular cracks, thereby contributing to the outstanding cycling performance (74% capacity retention over 2500 cycles at 10 C, 1 C = 170 mA g⁻¹). In addition, Ma's group reported the creation of a Na₃(VOP₄)₂F (NVOPF) coated NaMnHCF composite (PBM@NVOPF) through solution precipitation.¹⁴¹ The NASICON-type NVOPF with high chemical stability can undoubtedly protect NaMnHCF from the corrosion of HF formed in the electrolyte and inhibit the dissolution of active materials. Hence, excellent electrochemical performance at both room temperature (84.3% capacity retention after 500 cycles) and 55 °C (78.8% capacity retention after 200 cycles) could be acquired at the current density of 100 mA g⁻¹.

Moreover, the degradation of PBAs would induce cracks and even the collapse of the cathode–electrolyte interface (CEI), and the newly exposed surface could trigger new CEI formation. Eventually, a thick and uneven CEI was formed and the electrolyte was used up, leading to the death of SIBs. Therefore, it is of great significance to construct a stable and homogeneous CEI on the surface of PBAs to enhance the cycling stability of SIBs. Lately, Li's group created an artificial NaF-rich CEI via chemical presodiation between metallic Na, biphenyl, and 1,2-dimethoxyethane (DME), as illustrated in Figure 11c.¹³⁹ The Na⁺-conducting NaF-rich CEI effectively prevents CEI@PB from attacking organic solvents and contributes to the longer lifespan of coated PBAs compared to those of bare PBAs. More importantly, the uniformity was maintained, and the thickness of the CEI was approximately

4.8 nm after cycling, which was much smaller than that of PB (~22.6 nm).

4.1.4.2. Stable SE-PBAs Materials. Although the aforementioned inorganic coating layers have been proven effective, a lattice mismatch between PBAs and coating exists. Coating PBAs with compounds of similar lattice parameters will eliminate lattice mismatches to a greater extent. Among various PBAs with different transition metal ions, Ni-based PBAs (Ni-HCF) have been proven the most chemical/electrochemical stable materials with “zero strain” during cycling.¹⁴² Therefore, most research focused on preparing a core–shell composite with Ni-HCF as the outer shell to suppress lattice distortion, transition metal dissolution, and the side reactions between PBAs and the organic electrolyte, thus enhancing the electrochemical performance. Generally, the following three strategies have been adopted for Ni-HCF coating: (i) In situ deposition of Ni-HCF on the surface of PBAs through coprecipitation.^{143,144} (ii) In situ ion exchange. Given the fact that the Mn–C≡N–Fe group has a higher solubility constant than Ni-HCF, it is feasible to coat sodium nickel hexacyanoferrate (PBN) on the surface of sodium manganese hexacyanoferrate (PBM), as shown in Figure 11d.¹⁴⁵ (iii) One-pot synthesis to obtain epitaxial core–shell PBAs because of the unequal formation and stability constants of citrate anion for Ni²⁺ and Mn²⁺. Our group found that Ni²⁺ tends to be released only when Mn²⁺ is completely consumed, resulting in an epitaxial growth of NiPB on the already formed MnPB template.¹⁴⁵ Benefiting from the highly matched lattice parameters, NiPB exerted a stabilizing counterbalancing strain on the Jahn–Teller-distorted MnN₆ octahedra. As a result, the MnNiPB-4xcit with an optimized equivalent of Na₃Cit possessed an appropriate thickness (9% of thickness of MnPB) to imbue the material with phase stability and an ultrahigh capacity retention of 96% after 500 cycles.

4.1.4.3. Conductive Carbon/Polymers. Besides inorganic materials and Ni-HCF, conductive carbons/polymers, including reduced graphene oxide (rGO),^{146,147} polypyrrole (PPY),^{140,148} polydopamine (PDA),¹⁴⁹ polyaniline (PANI),¹⁵⁰ and poly(3,4-ethylene dioxythiophene) (PEDOT),¹⁵¹ could be applied as the coating layers. The conductive carbon/polymer coating has multiple merits: enhancing the overall electrical conductivity, suppressing the chemical dissolution, preventing unexpected attack of organic electrolyte, reducing the partially oxidized trivalent Fe³⁺/Mn³⁺ by in situ polymerization, and offering additional redox sites to increase the capacity of electrodes by some of the carbonaceous materials, such as PPY and PANI (Figure 11e).

4.1.5. Cationic Doping. Cationic doping (elemental substitution) has been proven to be effective strategy to enhance the capacity, working voltage, and cycling performance for cathode materials in SIBs. The same concept could be used for PBAs with partial substitution of the transition metal coordinated with a N atom (Fe atom coordinated with C is fixed in most cases) or an alkali element. It is confirmed that the species or amount of doping metal has a significant influence on the structural stability and electrochemical behavior of PBAs. Therefore, ingenious regulation of the doping level is crucial for electrochemical performance improvement.

The studies on transition metal doping are mainly focused on DE-PBAs (Fe-HCFs and Mn-HCFs) with high specific capacities but insufficient cycling performances, in which the N-coordinated Fe/Mn could be partially substituted by one or

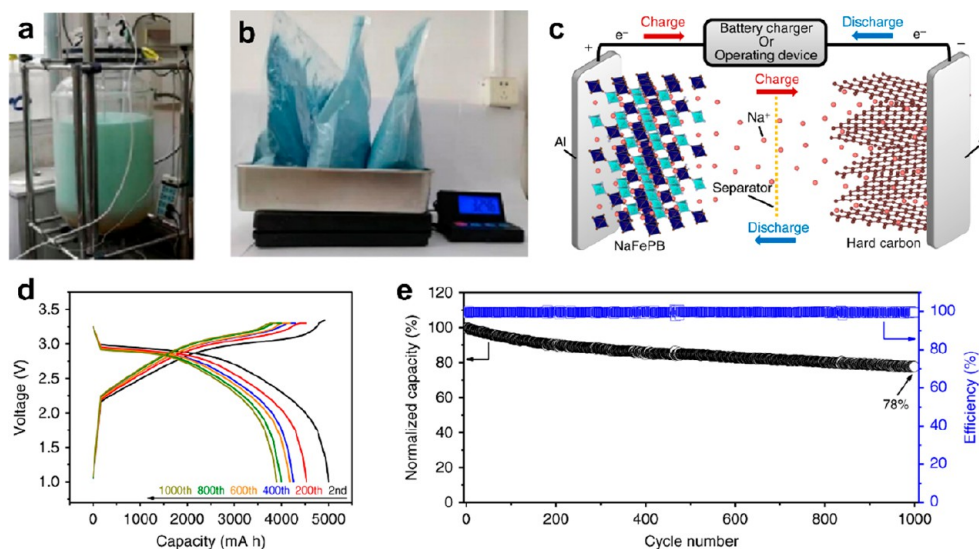


Figure 12. (a and b) Kilogram-grade preparation of MnFeNi-PB. Reproduced with permission from ref 177. Copyright 2022 Elsevier. (c) Working mechanism of a 5 Ah pouch full cell-based $\text{Na}_{2-x}\text{FeFe}(\text{CN})_6$ cathode and hard carbon anode, (d) charge–discharge curves, and (e) cycling performance of the 5 Ah pouch full cell. Reproduced with permission from ref 179. Copyright 2020 Springer Nature.

multiple elements to adjust the crystal structure and redox behaviors. For Fe-HCF, the low-spin Fe^{LS} redox at the higher voltage is hard to activate due to the existence of $[\text{Fe}(\text{CN})_6]$ vacancies. Through divalent Ni,^{152,153} Zn,¹⁵⁴ Cu,^{155,156} or Mn¹⁵⁷ doping, the capacity contribution of the low spin Fe^{LS} redox could be elevated to decrease the energy barriers of Na^+ migration. It was found that 3% Ni substitution in Fe-HCF could increase the low spin Fe^{LS} capacity contribution from 28% (27 mA h g^{-1}) to 43% (50 mA h g^{-1}).¹⁵² Meanwhile, Yang's group reported that 11% Zn substitution in FeZn-PB delivered a higher low spin Fe^{LS} capacity of 60.5 mA h g^{-1} , which was higher than that of Fe-PB (50 mA h g^{-1}) at current density of 20 mA g^{-1} .¹⁵⁴ In addition, it was demonstrated in our group that a sample with 36% Zn substitution shows minor lattice distortion for the simplified and reversible phase transition from cubic to tetragonal.¹⁵⁸ As for Mn-HCF, a dramatic capacity decay is observed due to the Jahn–Teller distortion of Mn^{3+} , and a 10% decrease in Mn–N distances could be detected after a full charge.^{159,160} The effects of doping Fe, Co, and Ni for the cycling and rate performance of Mn-HCF have been investigated in Shibata's group.¹⁶¹ They found that the lifespan and the capacity retention at high rate were significantly increased due to the suppressed Jahn–Teller distortion of Mn^{3+} . After that, He and coworkers reported that the phase structure of Mn-HCF would change from rhombohedral to cubic after Sn^{4+} doping, and enhanced capacity retention after 100 cycles at 240 mA g^{-1} was obtained (80.5% vs 54.0% for bare Mn-HCF).¹⁶² Lately, Jahn–Teller distortion was found by Shao' group to be repressed through employing Mn vacancies (V_{Mn}) in combination with Ni doping.¹⁶³

In order to further enhance the electrochemical performance, multication lattice substitution has been employed.^{164,165} High quality (HQ)- $\text{Ni}_x\text{Co}_{1-x}[\text{Fe}(\text{CN})_6]$ PBAs were synthesized through a chelating agent (trisodium citrate)/surfactant (polyvinylpyrrolidone, PVP) coassisted crystallization method with fewer $[\text{Fe}(\text{CN})_6]$ vacancies and water molecules in Han's group.¹⁶⁶ As a result, the optimized sample ($x = 0.3$) exhibited a high specific capacity of 145 mA h g^{-1} and prolonged cyclability of 90% capacity retention after 600 cycles. After

that, a ternary NiCoFe-PB sample with Co and Fe at the Ni site was prepared by Yang and coworkers. In such a unique electrode material, Co doping enhanced the redox activity of Fe^{LS} ; meanwhile, Fe doping enhanced the redox activity of Co^{HS} .¹⁶⁷ Additionally, FeCo-co-doping could reduce the Na^+ diffusion resistance within the solid electrolyte interface; thus, an ultralow capacity fading rate of 0.0044% per cycle has been obtained. Moreover, high-entropy PBAs cathode materials with FeMnNiCuCo sharing the N-coordinated M_1 site for SIB were first reported by Brezesinski's group.¹⁶⁸ The equimolar fractions of above five metal cations increased the structural stability and configurational entropy and suppressed the degradation of PBAs cathodes at high voltages. After that, a link between the high-entropy effect and the observed energy storage capabilities of Mn-HCF was established for the first time. By systematic comparison of the structural and chemical properties of high-, medium-, and low-entropy Mn-HCFs, Brezesinski and coworkers concluded that the electrochemical performance enhancement could be ascribed to the entropy-mediated suppression of the Jahn–Teller distortion.¹⁶⁹ Inspired by the disordered Rubik's cube, our group synthesized a high-entropy PBA sample as a “proof-of-concept” to demonstrate its application in energy storage devices.¹⁷⁰ It was revealed that the increased configuration entropy could promote thermal/air stability and afford a zero-strain two-phase (cubic \leftrightarrow tetragonal) Na^+ storage mechanism. As a consequence, the ultralong cycling lifespan over 50 000 cycles (a capacity retention of 79.2%) was achieved.

Owing to the large family of PBAs, the reversible (de)insertion of an alkali ion can be allowed, and K^+ insertion has been confirmed to exhibit the best reversibility with the highest potential.¹⁷¹ Therefore, most researchers are forced on K^+ doping to improve the structural and electrochemical stability.^{172,173} A low concentration of K^+ in $\text{Na}_x\text{K}_y\text{FeHCF}$ samples would expand the PBA framework structure and provide a larger cell volume for Na^+ intercalation.¹⁷⁴ In addition, K^+ could be reinserted at 8c sites before Na^+ , providing extra specific capacity and preventing the phase transition and lattice expansion. Then, the synthesis of a series of $\text{K}_x\text{Na}_y\text{MnFe}(\text{CN})_6$ ($x + y \leq 2$, KNMF) samples through

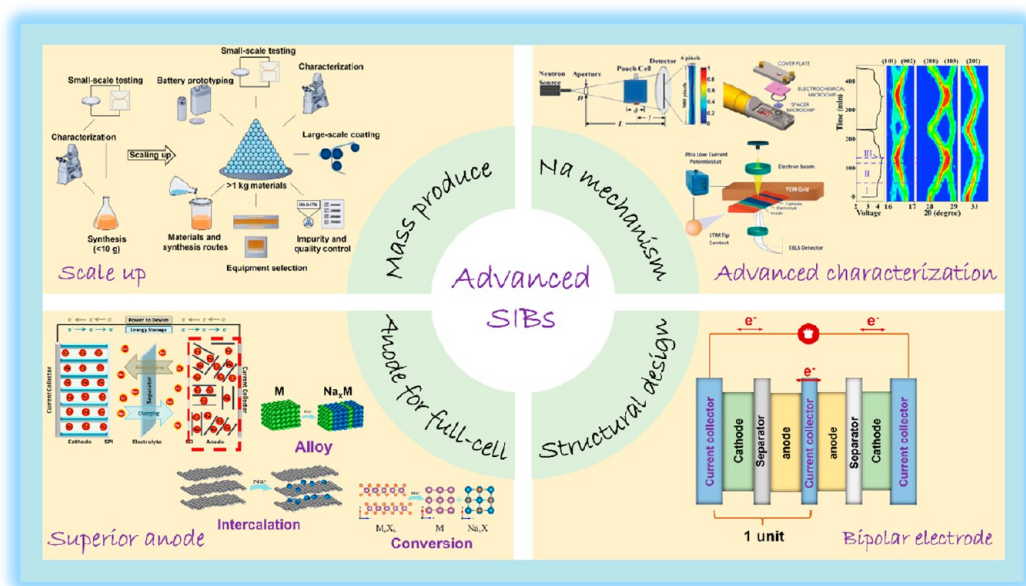


Figure 13. Figure for the development prospects of cathode materials in SIBs. Top left image reproduced with permission from ref 180. Copyright 2023 Springer Nature. Top right (center) image reproduced with permission from ref 181. Copyright 2019 Wiley-VCH. Far right image reproduced with permission from ref 185. Copyright 2021 Royal Society of Chemistry. Bottom left (center) image reproduced with permission from ref 186. Copyright 2023 American Chemical Society.

coprecipitation route was proposed by Qiao's group, where adjunctive sodium citrate was used as sodium resource and organic additive.¹⁷⁵ KNMF-3 ($x = 1.59$, $y = 0.25$) exhibited better electrochemical performance with good crystallinity, a high Na^+ content, and nanocubic morphology compared to the sample without K-doping. A facile "potassium-ions assisted" strategy was developed by our group to prepare highly crystallized Fe-based PBAs by controlling the crystal phase orientation.¹⁷⁶ The optimized product NKPB-3 ($\text{Na}_{0.28}\text{K}_{1.55}\text{Fe}[\text{Fe}(\text{CN})_6] \cdot 1.53\text{H}_2\text{O}$) displayed a stable structure-orientating (220) plane with fewer $[\text{Fe}(\text{CN})_6]_4$ vacancies and a lower water content. Attributed to the highly crystal structure and pillar effect of K^+ , the as-obtained electrode delivered a high initial specific capacity of 147.9 mA h g^{-1} and 83.5% capacity retention after 300 cycles.

In order to effectively enhance the doping measures for Fe-HCF materials, it is important to increase the redox activity of Fe^{LS} and the capacity contribution of the low spin Fe^{LS} . This can be achieved by incorporating alternative elements, such as Ni, Co, Zn, etc. For Mn-HCF, the key issue is to use the doped elements to limit the Jahn–Teller effect of Mn^{3+} and enhance the structural stability. In this strategy, elements such as Fe, Co, Ni, and Sn were adopted. It was worth noting the introduction of both Co and Ni, as they had dual effects, while taking into account their intake/cost. Furthermore, doping K^+ into the alkali site is an excellent practice that greatly improves the structural and electrochemical stability. Continuous regulation of the introduced solubility is necessary to achieve the best effect for future development.

4.2. Scalable Preparation. Up to now, several groups have begun to prepare PBAs cathode materials on a kilogram-scale. Xie's group synthesized the Ni and Fe-codoped manganese hexacyanoferrate PB (MnFeNi-PB) via a Na_3Cit -assisted coprecipitation method.¹⁷⁷ They realized kilogram-scale MnFeNi-PB using a 100 L reactor, and 3.2 kg of sample could be obtained, as shown in Figure 12a and b. The as-prepared MnFeNi-PB exhibited a long cycle life at room

temperature (65.5% capacity after 2000 cycles, 5 C, 1 C = 150 mA g^{-1}), 45 °C (83.5% capacity retention, 300 cycles, 1 C), and -20 °C (92.1% capacity retention, 700 cycles, 1 C). After that, they synthesized Mn/Ni binary PBAs in a high precursor salt concentration of 0.5 mol L^{-1} ($\text{Mn}_{0.5}\text{Ni}_{0.5-0.5}$), resulting in a higher yield for mass production.¹⁷⁸ The result showed that the cycling performance and discharge specific capacity were better than those of the sample prepared at a lower salt concentration. Moreover, $\text{Mn}_{0.5}\text{Ni}_{0.5-0.5}$ displayed excellent cycling performance at overcharge to 4.8 V (91.8% retention) and overdischarge to 1.2 V (89.1% retention) after 300 cycles, demonstrating that it exhibited a satisfactory tolerance for deep charge/discharge. In addition, sodium-rich $\text{Na}_{2-x}\text{FeFe}(\text{CN})_6$ has been successfully prepared in our group by a scale-up precipitation route with Na_3Cit as a chelating agent and sodium supplement (yield of 5 kg per 100 L).¹⁷⁹ It was concluded that Na_3Cit could play the most important role in crystal growth. With the increase of the Na_3Cit concentration, the morphology of $\text{Na}_{2-x}\text{FeFe}(\text{CN})_6$ turned to a single microcube compared to irregular particles at low concentration. Subsequently, A 5 Ah pouch full cell with an as-prepared $\text{Na}_{2-x}\text{FeFe}(\text{CN})_6$ cathode and hard carbon anode has been assembled, and excellent electrochemical behavior has been achieved (Figure 12c). Additionally, no sodium compensation was added because the sodium atomic ration in this Fe-PBA cathode reached up to 1.73. As shown in Figure 12d and e, an obvious plateau at 2.9 V was observed, and 78% capacity retention could be obtained after 1000 cycles. Such significant work can pave the way for scaled-up preparation of PBAs in the future.

5. OUTLOOK AND PERSPECTIVES

In summary, great progress has been made in developing cathode materials for SIBs in recent years in spite of the many challenges remaining. The commonly used cathode materials for SIBs include transition metal oxides, polyanion compounds,

and Prussian blue (analogs), which have different physical and chemical properties and electrochemical performance due to their versatile compositions and crystal structures. The transition metal oxides can be simply prepared and demonstrate high specific capacity and good rate capability, but they are prone to collapse during repeated Na insertion/extraction owing to their fragile crystal structures, which is usually resolved by lattice regulation. Polyanionic materials have high working voltages and excellent thermal/cyclic stability due to from their stable crystal structure and strong X–O polar bonds, but they suffer from inferior electronic conductivity. Surface modification and morphology/lattice regulation have been explored to improve the performance of polyanionic cathode. Prussian blue and its analogs have the advantages of low cost, great rate performance, and adjustable working voltages, but the stubborn crystal water causes their chemical and structural instability. In conclusion, there are remaining issues that need to be addressed before the above three categories of cathode materials showcase their grandeur in the field of large-scale energy storage, as discussed in below (Figure 13).

- (i) Developing large-scale synthesis techniques: Anode materials, such as hard carbon and silicon, can be easily mass produced with high consistency due to their simple compositions and abundant raw materials, while syntheses of cathodic materials containing complex components and expensive raw materials (e.g., V-, Cu-, and Co-based compositions) usually involve cumbersome synthesis steps, making the mass production of cathode materials highly challenging. Synthesis techniques such as the coprecipitation method and solid-state ball milling can be extended to large scale production with their product yields and batch stability further improved.
- (ii) In-depth understanding of the Na storage mechanism: The studies on the in situ structure/component evolution of the electrodes and the genesis of a cathode electrolyte interface (CEI) film during cycling are essential to illustrate the Na storage mechanism and guiding the development of the high performance cathode materials. Therefore, advanced characterization techniques, such as in situ neutron diffraction, in situ X-ray absorption spectroscopy (XAS), and in situ electrochemical monitoring, should be more intensively adopted.
- (iii) Seeking matching anodes for full-cell study: The assemble of a Na full cell must consider the matching between the cathode and the anode. High specific capacity is the ultimate pursuit in selecting anode materials, so traditional hard carbon anode materials with limited theoretical capacity cannot meet the needs of high-energy SIBs. Carbon-based anode materials with high specific capacities, such as graphene and carbon nanotubes, have been developed and applied to full cells of SIBs. In addition, alloy–carbon composites and sodium metal anodes are also under consideration, expecting the high expansion of the alloy anode and severe dendritic growth of the Na metal anode will be resolved in the near future.
- (iv) Optimizing the construction of SIBs: The bipolar electrode design using inexpensive aluminum as a shared current collector can help achieve efficient recycling of

electrode materials, and the absence of alloying reaction between Na and Al is the foundation of this design. Although the construction of SIBs with a bipolar electrode may render a lot of advantages, including higher specific (volumetric) energy density, excellent high-rate performance, and reduced cell resistance, potential electrolyte leakage and subsequent intermixing may cause exhaustive failure of the batteries. The validity and reliability of a variety of battery constructions have yet to be examined.

■ AUTHOR INFORMATION

Corresponding Authors

Shulei Chou – Institute for Carbon Neutralization, College of Chemistry and Materials Engineering, Wenzhou University, Wenzhou, Zhejiang 325035, China; Wenzhou Key Laboratory of Sodium-Ion Batteries, Wenzhou University Technology Innovation Institute for Carbon Neutralization, Wenzhou, Zhejiang 325035, China; orcid.org/0000-0003-1155-6082; Email: chou@wzu.edu.cn

Yan Yu – Hefei National Research Center for Physical Sciences at the Microscale, Department of Materials Science and Engineering, CAS Key Laboratory of Materials for Energy Conversion, University of Science and Technology of China, Hefei, Anhui 230026, China; orcid.org/0000-0002-3685-7773; Email: yanyumse@ustc.edu.cn

Authors

Shitan Xu – School of Materials and Energy, Guangdong University of Technology, Guangzhou, Guangdong 510006, China

Huanhuan Dong – Institute for Carbon Neutralization, College of Chemistry and Materials Engineering, Wenzhou University, Wenzhou, Zhejiang 325035, China; Wenzhou Key Laboratory of Sodium-Ion Batteries, Wenzhou University Technology Innovation Institute for Carbon Neutralization, Wenzhou, Zhejiang 325035, China

Dan Yang – School of Materials and Energy, Guangdong University of Technology, Guangzhou, Guangdong 510006, China

Chun Wu – Institute for Carbon Neutralization, College of Chemistry and Materials Engineering, Wenzhou University, Wenzhou, Zhejiang 325035, China; Wenzhou Key Laboratory of Sodium-Ion Batteries, Wenzhou University Technology Innovation Institute for Carbon Neutralization, Wenzhou, Zhejiang 325035, China; orcid.org/0000-0002-9783-1307

Yu Yao – Hefei National Research Center for Physical Sciences at the Microscale, Department of Materials Science and Engineering, CAS Key Laboratory of Materials for Energy Conversion, University of Science and Technology of China, Hefei, Anhui 230026, China

Xianhong Rui – School of Materials and Energy, Guangdong University of Technology, Guangzhou, Guangdong 510006, China; orcid.org/0000-0003-1125-0905

Complete contact information is available at:

<https://pubs.acs.org/10.1021/acscentsci.3c01022>

Author Contributions

[‡]S.X. and H.D. contributed equally to this work.

Notes

The authors declare no competing financial interest.

ACKNOWLEDGMENTS

This work was supported by the National Natural Science Foundation of China (nos. 51925207, 52161145101, U1910210, 52250710680, 51971124, 52171217, 52101265, 52202284, and 22209123), the “Transformational Technologies for Clean Energy and Demonstration” Strategic Priority Research Program of Chinese Academy of Sciences (Grant XDA21000000), the National Synchrotron Radiation Laboratory (KY2060000173), the Joint Fund of the Yulin University and the Dalian National Laboratory for Clean Energy (Grant. YLU-DNL Fund 2021002), the Zhejiang Natural Science Foundation (LQ23E020002), and the Wenzhou Natural Science Foundation (G20220019).

REFERENCES

- (1) Xu, M.; Liu, M.; Yang, Z.; Wu, C.; Qian, J. Research Progress on Presodiation Strategies for High Energy Sodium-Ion Batteries. *Acta Phys. -Chim. Sin.* **2022**, *39*, 2210043.
- (2) Li, Q.; Yang, D.; Chen, H.; Lv, X.; Jiang, Y.; Feng, Y.; Rui, X.; Yu, Y. Advances in Metal Phosphides for Sodium-Ion Batteries. *SusMat* **2021**, *1*, 359–392.
- (3) Zhao, C. L.; Wang, Q. D.; Yao, Z. P.; Wang, J. L.; Sanchez-Lengeling, B.; Ding, F. X.; Qi, X. G.; Lu, Y. X.; Bai, X. D.; Li, B. H.; et al. Rational Design of Layered Oxide Materials for Sodium-Ion Batteries. *Science* **2020**, *370*, 708–711.
- (4) Gabriel, E.; Ma, C.; Graff, K.; Conrado, A.; Hou, D.; Xiong, H. Heterostructure Engineering in Electrode Materials for Sodium Ion Batteries: Recent Progress and Perspectives. *eScience* **2023**, 100139.
- (5) Xia, X.; Xu, S.; Tang, F.; Yao, Y.; Wang, L.; Liu, L.; He, S.; Yang, Y.; Sun, W.; Xu, C.; et al. A Multifunctional Interphase Layer Enabling Superior Sodium-Metal Batteries under Ambient Temperature and -40 degrees C. *Adv. Mater.* **2023**, *35*, 2209511.
- (6) Liu, Q. N.; Hu, Z.; Chen, M. Z.; Zou, C.; Jin, H. L.; Wang, S.; Chou, S. L.; Liu, Y.; Dou, S. X. The Cathode Choice for Commercialization of Sodium-Ion Batteries: Layered Transition Metal Oxides versus Prussian Blue Analogs. *Adv. Funct. Mater.* **2020**, *30*, 1909530.
- (7) Song, T.; Wang, C.; Lee, C. Structural Degradation Mechanisms and Modulation Technologies of Layered Oxide Cathodes for Sodium-Ion Batteries. *Carbon Neutralization* **2022**, *1*, 68–92.
- (8) Wang, Q.; Chu, S.; Guo, S. Progress on Multiphase Layered Transition Metal Oxide Cathodes of Sodium Ion Batteries. *Chin. Chem. Lett.* **2020**, *31*, 2167–2176.
- (9) Barpanda, P.; Lander, L.; Nishimura, S.-i.; Yamada, A. Polyanionic Insertion Materials for Sodium-Ion Batteries. *Adv. Energy Mater.* **2018**, *8*, 1703055.
- (10) Jin, T.; Li, H.; Zhu, K.; Wang, P. F.; Liu, P.; Jiao, L. Polyanion-Type Cathode Materials for Sodium-Ion Batteries. *Chem. Soc. Rev.* **2020**, *49*, 2342–2377.
- (11) Niu, Y.; Zhao, Y.; Xu, M. Manganese-Based Polyanionic Cathodes for Sodium-Ion Batteries. *Carbon Neutralization* **2023**, *2*, 150–168.
- (12) Qian, J. F.; Wu, C.; Cao, Y. L.; Ma, Z. F.; Huang, Y. H.; Ai, X. P.; Yang, H. X. Prussian Blue Cathode Materials for Sodium-Ion Batteries and Other Ion Batteries. *Adv. Energy Mater.* **2018**, *8*, 1702619.
- (13) Gan, L.; Yuan, X.; Han, J.; Li, J.; Zheng, L.; Yao, H. The Synergy of Dis-/ordering Ensures the Superior Comprehensive Performance of P2-Type Na-Based Layered Oxide Cathodes. *Carbon Neutralization* **2023**, *2*, 235–244.
- (14) Susanto, D.; Cho, M. K.; Ali, G.; Kim, J.-Y.; Chang, H. J.; Kim, H.-S.; Nam, K.-W.; Chung, K. Y. Anionic Redox Activity as a Key Factor in the Performance Degradation of NaFeO₂ Cathodes for Sodium Ion Batteries. *Chem. Mater.* **2019**, *31*, 3644–3651.
- (15) Wang, L.; Wang, J.; Zhang, X.; Ren, Y.; Zuo, P.; Yin, G.; Wang, J. Unravelling the Origin of Irreversible Capacity Loss in NaNiO₂ for High Voltage Sodium Ion Batteries. *Nano Energy* **2017**, *34*, 215–223.
- (16) Yabuuchi, N.; Yano, M.; Yoshida, H.; Kuze, S.; Komaba, S. Synthesis and Electrode Performance of O3-Type NaFeO₂-NaNi_{1/2}Mn_{1/2}O₂ Solid Solution for Rechargeable Sodium Batteries. *J. Electrochem. Soc.* **2013**, *160*, A3131.
- (17) Kumakura, S.; Tahara, Y.; Kubota, K.; Chihara, K.; Komaba, S. Sodium and Manganese Stoichiometry of P2-Type Na_{2/3}MnO₂. *Angew. Chem., Int. Ed.* **2016**, *55*, 12760–12763.
- (18) Fang, Y.; Yu, X. Y.; Lou, X. W. A Practical High-Energy Cathode for Sodium-Ion Batteries Based on Uniform P2-Na_{0.7}CoO₂ Microspheres. *Angew. Chem., Int. Ed.* **2017**, *56*, 5801–5805.
- (19) Huang, Y.; Yan, Z.; Luo, W.; Hu, Z.; Liu, G.; Zhang, L.; Yang, X.; Ou, M.; Liu, W.; Huang, L.; et al. Vitalization of P2-Na_{2/3}Ni_{1/3}Mn_{2/3}O₂ at High-Voltage Cyclability via Combined Structural Modulation for Sodium-Ion Batteries. *Energy Storage Mater.* **2020**, *29*, 182–189.
- (20) Tapia-Ruiz, N.; Armstrong, A. R.; Alptekin, H.; Amores, M. A.; Au, H.; Barker, J.; Boston, R.; Brant, W. R.; Brittain, J. M.; Chen, Y.; et al. 2021 Roadmap for Sodium-Ion Batteries. *J. Phys. Energy* **2021**, *3*, 031503.
- (21) Hu, X.; Zhao, Z.; Wang, L.; Li, J.; Wang, C.; Zhao, Y.; Jin, H. VO₂ (A)/Graphene Nanostructure: Stand up to Na Ion Intercalation/Deintercalation for Enhanced Electrochemical Performance as a Na-Ion Battery Cathode. *Electrochim. Acta* **2019**, *293*, 97–104.
- (22) Murphy, D.; Christian, P. Solid State Electrodes for High Energy Batteries. *Science* **1979**, *205*, 651–656.
- (23) Popuri, S. R.; Miclau, M.; Artemenko, A.; Labrugere, C.; Villesuzanne, A.; Pollet, M. I. Rapid Hydrothermal Synthesis of VO₂ (B) and Its Conversion to Thermochromic VO₂ (M1). *Inorg. Chem.* **2013**, *52*, 4780–4785.
- (24) Wei, Q.; Liu, J.; Feng, W.; Sheng, J.; Tian, X.; He, L.; An, Q.; Mai, L. Hydrated Vanadium Pentoxide with Superior Sodium Storage Capacity. *J. Mater. Chem. A* **2015**, *3*, 8070–8075.
- (25) Dong, Y.; Li, S.; Zhao, K.; Han, C.; Chen, W.; Wang, B.; Wang, L.; Xu, B.; Wei, Q.; Zhang, L.; et al. Hierarchical Zigzag Na_{1.25}V₃O₈ Nanowires with Topotactically Encoded Superior Performance for Sodium-Ion Battery Cathodes. *Energy Environ. Sci.* **2015**, *8*, 1267–1275.
- (26) Kang, H.; Liu, Y.; Shang, M.; Lu, T.; Wang, Y.; Jiao, L. NaV₃O₈ Nanosheet@Polypyrrole Core-Shell Composites with Good Electrochemical Performance as Cathodes for Na-Ion Batteries. *Nanoscale* **2015**, *7*, 9261–9267.
- (27) Lee, Y.; Oh, S. M.; Park, B.; Ye, B. U.; Lee, N. S.; Baik, J. M.; Hwang, S. J.; Kim, M. H. Unidirectional Growth of Single Crystalline β -Na_{0.33}V₂O₅ and α -V₂O₅ Nanowires Driven by Controlling the pH of Aqueous Solution and Their Electrochemical Performances for Na-Ion Batteries. *CrystEngComm* **2017**, *19*, 5028–5037.
- (28) Moretti, A.; Maroni, F.; Osada, I.; Nobili, F.; Passerini, S. V₂O₅ Aerogel as a Versatile Cathode Material for Lithium and Sodium Batteries. *ChemElectroChem* **2015**, *2*, 529–537.
- (29) Liu, S.; Tong, Z.; Zhao, J.; Liu, X.; Wang, J.; Ma, X.; Chi, C.; Yang, Y.; Liu, X.; Li, Y. Rational Selection of Amorphous or Crystalline V₂O₅ Cathode for Sodium-Ion Batteries. *Phys. Chem. Chem. Phys.* **2016**, *18*, 25645–25654.
- (30) Su, D.; Ahn, H. J.; Wang, G. Hydrothermal Synthesis of α -MnO₂ and β -MnO₂ Nanorods as High Capacity Cathode Materials for Sodium Ion Batteries. *J. Mater. Chem. A* **2013**, *1*, 4845–4850.
- (31) Lu, K.; Hu, Z.; Xiang, Z.; Ma, J.; Song, B.; Zhang, J.; Ma, H. Cation Intercalation in Manganese Oxide Nanosheets: Effects on Lithium and Sodium Storage. *Angew. Chem.* **2016**, *128*, 10604–10608.
- (32) Silván, B.; Gonzalo, E.; Djuandhi, L.; Sharma, N.; Fauth, F.; Saurel, D. On the Dynamics of Transition Metal Migration and Its Impact on the Performance of Layered Oxides for Sodium-Ion Batteries: NaFeO₂ as a Case Study. *J. Mater. Chem. A* **2018**, *6*, 15132–15146.
- (33) Lee, E.; Brown, D. E.; Alp, E. E.; Ren, Y.; Lu, J.; Woo, J.-J.; Johnson, C. S. New Insights into the Performance Degradation of Fe-Based Layered Oxides in Sodium-Ion Batteries: Instability of Fe³⁺/Fe⁴⁺ Redox in α -NaFeO₂. *Chem. Mater.* **2015**, *27*, 6755–6764.

- (34) Thorne, J.; Zheng, L.; Lee, C. L.; Dunlap, R.; Obrovac, M. Synthesis and Electrochemistry of O3-Type NaFeO₂-NaCo_{0.5}Ni_{0.5}O₂ Solid Solutions for Na-Ion Positive Electrodes. *ACS Appl. Mater. Interfaces* **2018**, *10*, 22013–22022.
- (35) Kaufman, J. L.; Van der Ven, A. Na_xCoO₂ Phase Stability and Hierarchical Orderings in the O3/P3 Structure Family. *Phys. Rev. Mater.* **2019**, *3*, 015402.
- (36) Bianchini, M.; Wang, J.; Clément, R.; Ceder, G. A First-Principles and Experimental Investigation of Nickel Solubility into the P2 Na_xCoO₂ Sodium-Ion Cathode. *Adv. Energy Mater.* **2018**, *8*, 1801446.
- (37) Carlier, D.; Cheng, J.; Berthelot, R.; Guignard, M.; Yoncheva, M.; Stoyanova, R.; Hwang, B.; Delmas, C. The P2-Na_{2/3}Co_{2/3}Mn_{1/3}O₂ Phase: Structure, Physical Properties and Electrochemical Behavior as Positive Electrode in Sodium Battery. *Dalton Trans.* **2011**, *40*, 9306–9312.
- (38) Braconnier, J. J.; Delmas, C.; Fouassier, C.; Hagenmuller, P. Comportement Electrochimique Des Phases Na_xCoO₂. *Mater. Res. Bull.* **1980**, *15*, 1797–1804.
- (39) Clément, R. J.; Bruce, P. G.; Grey, C. P. Manganese-Based P2-Type Transition Metal Oxides as Sodium-Ion Battery Cathode Materials. *J. Electrochem. Soc.* **2015**, *162*, A2589.
- (40) Mendiboure, A.; Delmas, C.; Hagenmuller, P. Electrochemical Intercalation and Deintercalation of Na_xMnO₂ Bronzes. *J. Solid State Chem.* **1985**, *57*, 323–331.
- (41) Liu, X.; Zhong, G.; Xiao, Z.; Zheng, B.; Zuo, W.; Zhou, K.; Liu, H.; Liang, Z.; Xiang, Y.; Chen, Z.; et al. Al and Fe-Containing Mn-Based Layered Cathode with Controlled Vacancies for High-Rate Sodium Ion Batteries. *Nano Energy* **2020**, *76*, 104997.
- (42) Buchholz, D.; Chagas, L. G.; Vaalma, C.; Wu, L.; Passerini, S. Water Sensitivity of Layered P2/P3-Na_xNi_{0.22}Co_{0.11}Mn_{0.66}O₂ Cathode Material. *J. Mater. Chem. A* **2014**, *2*, 13415–13421.
- (43) Lu, Z.; Dahn, J. Intercalation of Water in P2, T2 and O2 Structure A₂[Co_xNi_{1/3-x}Mn_{2/3}]O₂. *Chem. Mater.* **2001**, *13*, 1252–1257.
- (44) You, Y.; Dolocan, A.; Li, W.; Manthiram, A. Understanding the Air-Exposure Degradation Chemistry at a Nanoscale of Layered Oxide Cathodes for Sodium-Ion Batteries. *Nano Lett.* **2019**, *19*, 182–188.
- (45) Zheng, L.; Li, L.; Shunmugasundaram, R.; Obrovac, M. Effect of Controlled-Atmosphere Storage and Ethanol Rinsing on NaNi_{0.5}Mn_{0.5}O₂ for Sodium-Ion Batteries. *ACS Appl. Mater. Interfaces* **2018**, *10*, 38246–38254.
- (46) Guignard, M.; Didier, C.; Darriet, J.; Bordet, P.; Elkaim, E.; Delmas, C. P2-Na_xVO₂ System as Electrodes for Batteries and Electron-Correlated Materials. *Nat. Mater.* **2013**, *12*, 74–80.
- (47) Delmas, C.; Fouassier, C.; Hagenmuller, P. Structural Classification and Properties of the Layered Oxides. *Physica B+C* **1980**, *99*, 81–85.
- (48) Xi, K.; Chu, S.; Zhang, X.; Zhang, X.; Zhang, H.; Xu, H.; Bian, J.; Fang, T.; Guo, S.; Liu, P.; et al. A high-Performance Layered Cr-Based Cathode for Sodium-Ion Batteries. *Nano Energy* **2020**, *67*, 104215.
- (49) Zheng, L.; Bennett, J. C.; Obrovac, M. Stabilizing NaCrO₂ by Sodium Site Doping with Calcium. *J. Electrochem. Soc.* **2019**, *166*, A2058.
- (50) Nam, K. W.; Kim, S.; Yang, E.; Jung, Y.; Levi, E.; Aurbach, D.; Choi, J. W. Critical Role of Crystal Water for a Layered Cathode Material in Sodium Ion Batteries. *Chem. Mater.* **2015**, *27*, 3721–3725.
- (51) Zuo, W.; Innocenti, A.; Zarrabeitia, M.; Bresser, D.; Yang, Y.; Passerini, S. Layered Oxide Cathodes for Sodium-Ion Batteries: Storage Mechanism, Electrochemistry, and Techno-economics. *Acc. Chem. Res.* **2023**, *56*, 284–296.
- (52) Sun, H. H.; Hwang, J. Y.; Yoon, C. S.; Heller, A.; Mullins, C. B. Capacity Degradation Mechanism and Cycling Stability Enhancement of AlF₃-Coated Nanorod Gradient Na[Ni_{0.65}Co_{0.08}Mn_{0.27}]O₂ Cathode for Sodium-Ion Batteries. *ACS Nano* **2018**, *12*, 12912–12922.
- (53) Li, J.; Hu, H.; Wang, J.; Xiao, Y. Surface Chemistry Engineering of Layered Oxide Cathodes for Sodium-Ion Batteries. *Carbon Neutralization* **2022**, *1*, 96–116.
- (54) Zuo, W.; Liu, X.; Qiu, J.; Zhang, D.; Xiao, Z.; Xie, J.; Ren, F.; Wang, J.; Li, Y.; Ortiz, G. F.; et al. Engineering Na⁺-Layer Spacings to Stabilize Mn-Based Layered Cathodes for Sodium-Ion Batteries. *Nat. Commun.* **2021**, *12*, 4903.
- (55) Jiang, L. W.; Lu, Y. X.; Wang, Y. S.; Liu, L. L.; Qi, X. G.; Zhao, C. L.; Chen, L. Q.; Hu, Y. S. A high-Temperature β-Phase NaMnO₂ Stabilized by Cu Doping and Its Na Storage Properties. *Chin. Phys. Lett.* **2018**, *35*, 048801.
- (56) Tsuchiya, Y.; Takanashi, K.; Nishinobo, T.; Hokura, A.; Yonemura, M.; Matsukawa, T.; Ishigaki, T.; Yamanaka, K.; Ohta, T.; Yabuuchi, N. Layered Na_xCr_xTi_{1-x}O₂ as Bifunctional Electrode Materials for Rechargeable Sodium Batteries. *Chem. Mater.* **2016**, *28*, 7006–7016.
- (57) Guo, S.; Liu, P.; Yu, H.; Zhu, Y.; Chen, M.; Ishida, M.; Zhou, H. A Layered P2-and O3-Type Composite as a High-Energy Cathode for Rechargeable Sodium-Ion Batteries. *Angew. Chem., Int. Ed.* **2015**, *54*, 5894–5899.
- (58) Li, Z. Y.; Zhang, J.; Gao, R.; Zhang, H.; Zheng, L.; Hu, Z.; Liu, X. Li-Substituted Co-Free Layered P2/O3 Biphasic Na_{0.67}Mn_{0.55}Ni_{0.25}Ti_{0.2-x}Li_xO₂ as High-Rate-Capability Cathode Materials for Sodium Ion Batteries. *J. Phys. Chem. C* **2016**, *120*, 9007–9016.
- (59) Qi, X.; Liu, L.; Song, N.; Gao, F.; Yang, K.; Lu, Y.; Yang, H.; Hu, Y. S.; Cheng, Z. H.; Chen, L. Design and Comparative Study of O3/P2 Hybrid Structures for Room Temperature Sodium-Ion Batteries. *ACS Appl. Mater. Interfaces* **2017**, *9*, 40215–40223.
- (60) Konarov, A.; Choi, J. U.; Bakenov, Z.; Myung, S. T. Revisit of Layered Sodium Manganese Oxides: Achievement of High Energy by Ni Incorporation. *J. Mater. Chem. A* **2018**, *6*, 8558–8567.
- (61) Wang, P. F.; Yao, H. R.; Liu, X. Y.; Yin, Y. X.; Zhang, J. N.; Wen, Y.; Yu, X.; Gu, L.; Guo, Y. G. Na⁺/Vacancy Disorder Promises High-Rate Na-Ion Batteries. *Sci. Adv.* **2018**, *4*, No. eaar6018.
- (62) Yabuuchi, N.; Hara, R.; Kajiyama, M.; Kubota, K.; Ishigaki, T.; Hoshikawa, A.; Komaba, S. New O2/P2-type Li-Excess Layered Manganese Oxides as Promising Multi-Functional Electrode Materials for Rechargeable Li/Na Batteries. *Adv. Energy Mater.* **2014**, *4*, 1301453.
- (63) Hemalatha, K.; Jayakumar, M.; Bera, P.; Prakash, A. Improved Electrochemical Performance of Na_{0.67}MnO₂ through Ni and Mg Substitution. *J. Mater. Chem. A* **2015**, *3*, 20908–20912.
- (64) Chae, M. S.; Kim, H. J.; Lyoo, J.; Attias, R.; Gofer, Y.; Hong, S. T.; Aurbach, D. Anomalous Sodium Storage Behavior in Al/F Dual-Doped P2-Type Sodium Manganese Oxide Cathode for Sodium-Ion Batteries. *Adv. Energy Mater.* **2020**, *10*, 2002205.
- (65) Yuan, D.; Liang, X.; Wu, L.; Cao, Y.; Ai, X.; Feng, J.; Yang, H. A Honeycomb-Layered Na₃Ni₂SbO₆: A high-rate and cycle-stable cathode for sodium-ion batteries. *Adv. Mater.* **2014**, *26*, 6301–6306.
- (66) Mariyappan, S.; Marchandier, T.; Rabuel, F.; Iadecola, A.; Rouse, G.; Morozov, A. V.; Abakumov, A. M.; Tarascon, J.-M. The Role of Divalent (Zn²⁺/Mg²⁺/Cu²⁺) Substituents in Achieving Full Capacity of Sodium Layered Oxides for Na-Ion Battery Applications. *Chem. Mater.* **2020**, *32*, 1657–1666.
- (67) Xu, Y.-S.; Gao, J. C.; Tao, X.-S.; Sun, Y. G.; Liu, Y.; Cao, A. M.; Wan, L. J. High-Performance Cathode of Sodium-Ion Batteries Enabled by A Potassium-Containing Framework of K_{0.5}Mn_{0.7}Fe_{0.2}Ti_{0.1}O₂. *ACS Appl. Mater. Interfaces* **2020**, *12*, 15313–15319.
- (68) Shi, Q.; Qi, R.; Feng, X.; Wang, J.; Li, Y.; Yao, Z.; Wang, X.; Li, Q.; Lu, X.; Zhang, J.; et al. Niobium-Doped Layered Cathode Material for High-Power and Low-Temperature Sodium-Ion Batteries. *Nat. Commun.* **2022**, *13*, 3205.
- (69) Rost, C. M.; Sacht, E.; Borman, T.; Moballegh, A.; Dickey, E. C.; Hou, D.; Jones, J. L.; Curtarolo, S.; Maria, J.-P. Entropy-Stabilized Oxides. *Nat. Commun.* **2015**, *6*, 8485.

- (70) Zhao, C.; Ding, F.; Lu, Y.; Chen, L.; Hu, Y. S. High-Entropy Layered Oxide Cathodes for Sodium-Ion Batteries. *Angew. Chem., Int. Ed.* **2020**, *59*, 264–269.
- (71) Yao, L.; Zou, P.; Wang, C.; Jiang, J.; Ma, L.; Tan, S.; Beyer, K. A.; Xu, F.; Hu, E.; Xin, H. L. High-Entropy and Superstructure-Stabilized Layered Oxide Cathodes for Sodium-Ion Batteries. *Adv. Energy Mater.* **2022**, *12*, 2201989.
- (72) Su, B.; Wu, S.; Liang, H.; Zhou, W.; Liu, J.; Goonetilleke, D.; Sharma, N.; Sit, P. H.-L.; Zhang, W.; Yu, D. Y. High-Performance NaVO_3 with Mixed Cationic and Anionic Redox Reactions for Na-Ion Battery Applications. *Chem. Mater.* **2020**, *32*, 8836–8844.
- (73) de Boisse, B. M.; Reynaud, M.; Ma, J.; Kikkawa, J.; Nishimura, S.-i.; Casas-Cabanas, M.; Delmas, C.; Okubo, M.; Yamada, A. Coulombic Self-Ordering upon Charging A Large-Capacity Layered Cathode Material for Rechargeable Batteries. *Nat. Commun.* **2019**, *10*, 2185.
- (74) Bai, X.; Sathiyaraj, M.; Mendoza-Sánchez, B.; Iadecola, A.; Vergnet, J.; Dedryvère, R.; Saubanière, M.; Abakumov, A. M.; Rozier, P.; Tarascon, J. M. Anionic Redox Activity in a Newly Zn-Doped Sodium Layered Oxide $\text{P2-Na}_{2/3}\text{Mn}_{1-y}\text{Zn}_y\text{O}_2$ ($0 < y < 0.23$). *Adv. Energy Mater.* **2018**, *8*, 1802379.
- (75) Rong, X.; Hu, E.; Lu, Y.; Meng, F.; Zhao, C.; Wang, X.; Zhang, Q.; Yu, X.; Gu, L.; Hu, Y. S.; et al. Anionic Redox Reaction-Induced High-Capacity and Low-Strain Cathode with Suppressed Phase Transition. *Joule* **2019**, *3*, 503–517.
- (76) Kim, D.; Lee, J. Anionic Redox Reactions in Manganese-Based Binary Layered Oxides for Advanced Sodium-Ion Batteries. *Chem. Mater.* **2020**, *32*, 5541–5549.
- (77) Ding, F. X.; Zhao, C. L.; Zhou, D.; Meng, Q. S.; Xiao, D. D.; Zhang, Q. Q.; Niu, Y. S.; Li, Y. Q.; Rong, X. H.; Lu, Y. X.; et al. A Novel Ni-Rich $\text{O3-Na}[\text{Ni}_{0.66}\text{Fe}_{0.25}\text{Mn}_{0.15}]\text{O}_2$ Cathode for Na-Ion Batteries. *Energy Storage Mater.* **2020**, *30*, 420–430.
- (78) Masquelier, C.; Croguennec, L. Polyanionic (Phosphates, Silicates, Sulfates) Frameworks as Electrode Materials for Rechargeable Li (or Na) Batteries. *Chem. Rev.* **2013**, *113*, 6552–6591.
- (79) Cao, X.; Zhou, J.; Pan, A.; Liang, S. Recent Advances in Phosphate Cathode Materials for Sodium-ion Batteries. *Acta Phys. Chim. Sin.* **2020**, *36*, 1905018.
- (80) Barpanda, P.; Oyama, G.; Nishimura, S.; Chung, S. C.; Yamada, A. A 3.8-V Earth-Abundant Sodium Battery Electrode. *Nat. Commun.* **2014**, *5*, 4358.
- (81) Bianchini, F.; Fjellvag, H.; Vajeeston, P. First-Principles Study of the Structural Stability and Electrochemical Properties of Na_2MSiO_4 ($M = \text{Mn, Fe, Co and Ni}$) Polymorphs. *Phys. Chem. Chem. Phys.* **2017**, *19*, 14462–14470.
- (82) Li, S.; Guo, J.; Ye, Z.; Zhao, X.; Wu, S.; Mi, J. X.; Wang, C. Z.; Gong, Z.; McDonald, M. J.; Zhu, Z.; et al. Zero-Strain $\text{Na}_2\text{FeSiO}_4$ as Novel Cathode Material for Sodium-Ion Batteries. *ACS Appl. Mater. Interfaces* **2016**, *8*, 17233–17238.
- (83) Strauss, F.; Rouse, G.; Sougrati, M. T.; Dalla Corte, D. A.; Curtzy, M.; Dominko, R.; Tarascon, J. M. Synthesis, Structure, and Electrochemical Properties of $\text{Na}_3\text{MB}_2\text{O}_{10}$ ($M = \text{Fe, Co}$) Containing M^{2+} in Tetrahedral Coordination. *Inorg. Chem.* **2016**, *55*, 12775–12782.
- (84) Li, J. J.; Kuang, Q.; Wen, N.; Yao, H.; Wu, J.; Fan, Q. H.; Dong, Y. Z.; Zhao, Y. M. Dual-Carbon Decorated $\text{Na}_3\text{Mn}_2(\text{P}_2\text{O}_7)(\text{PO}_4)$ Nanocomposite via Freeze Drying: A Zero-Strain Cathode Material for Sodium Ion Batteries. *J. Power Sources* **2022**, *521*, 230927.
- (85) Xu, S.; Yang, Y.; Tang, F.; Yao, Y.; Lv, X.; Liu, L.; Xu, C.; Feng, Y.; Rui, X.; Yu, Y. Vanadium Fluorophosphates: Advanced Cathode Materials for Next-Generation Secondary Batteries. *Mater. Horiz.* **2023**, *10*, 1901–1923.
- (86) Zhu, L.; Wang, H.; Sun, D.; Tang, Y.; Wang, H. A Comprehensive Review on the Fabrication, Modification and Applications of $\text{Na}_3\text{V}_2(\text{PO}_4)_2\text{F}_3$ Cathodes. *J. Mater. Chem. A* **2020**, *8*, 21387–21407.
- (87) Zhang, X.; Rui, X.; Chen, D.; Tan, H.; Yang, D.; Huang, S.; Yu, Y. $\text{Na}_3\text{V}_2(\text{PO}_4)_3$: An Advanced Cathode for Sodium-Ion Batteries. *Nanoscale* **2019**, *11*, 2556–2576.
- (88) Jungers, T.; Mahmoud, A.; Malherbe, C.; Boschini, F.; Vertruyen, B. Sodium Iron Sulfate Alluaudite Solid Solution for Na-Ion Batteries: Moving towards Stoichiometric $\text{Na}_2\text{Fe}_2(\text{SO}_4)_3$. *J. Mater. Chem. A* **2019**, *7*, 8226–8233.
- (89) Kim, H.; Park, I.; Seo, D. H.; Lee, S.; Kim, S. W.; Kwon, W. J.; Park, Y. U.; Kim, C. S.; Jeon, S.; Kang, K. New Iron-Based Mixed-Polyanion Cathodes for Lithium and Sodium Rechargeable Batteries: Combined First Principles Calculations and Experimental Study. *J. Am. Chem. Soc.* **2012**, *134*, 10369–10372.
- (90) Rui, X.; Sun, W.; Wu, C.; Yu, Y.; Yan, Q. An Advanced Sodium-Ion Battery Composed of Carbon Coated $\text{Na}_3\text{V}_2(\text{PO}_4)_3$ in a Porous Graphene Network. *Adv. Mater.* **2015**, *27*, 6670–6676.
- (91) Xiong, H. L.; Sun, G.; Liu, Z. L.; Zhang, L.; Li, L.; Zhang, W.; Du, F.; Qiao, Z. A. Polymer Stabilized Droplet Templating towards Tunable Hierarchical Porosity in Single Crystalline $\text{Na}_3\text{V}_2(\text{PO}_4)_3$ for Enhanced Sodium-Ion Storage. *Angew. Chem., Int. Ed.* **2021**, *60*, 10334–10341.
- (92) Wei, Q. L.; Chang, X. Q.; Wang, J.; Huang, T. Y.; Huang, X. J.; Yu, J. Y.; Zheng, H. F.; Chen, J. H.; Peng, D. L. An Ultrahigh-Power Mesocarbon Microbeads/ Na^+ -Diglyme/ $\text{Na}_3\text{V}_2(\text{PO}_4)_3$ Sodium-Ion Battery. *Adv. Mater.* **2022**, *34*, 2108304.
- (93) Liang, L. W.; Li, X. Y.; Zhao, F.; Zhang, J. Y.; Liu, Y.; Hou, L. R.; Yuan, C. Z. Construction and Operating Mechanism of High-Rate Mo-Doped $\text{Na}_3\text{V}_2(\text{PO}_4)_3$ @C Nanowires toward Practicable Wide-Temperature-Tolerance Na-Ion and Hybrid Li/Na-Ion Batteries. *Adv. Energy Mater.* **2021**, *11*, 2100287.
- (94) Shi, H.; Chen, Y.; Li, J.; Guo, L. Outstanding Long Cycle Stability Provide by Bismuth Doped $\text{Na}_3\text{V}_2(\text{PO}_4)_3$ Enwrapped with Carbon Nanotubes Cathode for Sodium-Ion Batteries. *J. Colloid Interface Sci.* **2023**, *652*, 195–207.
- (95) Li, H.; Jin, T.; Chen, X.; Lai, Y.; Zhang, Z.; Bao, W.; Jiao, L. Rational Architecture Design Enables Superior Na Storage in Greener NASICON $\text{Na}_4\text{MnV}(\text{PO}_4)_3$ Cathode. *Adv. Energy Mater.* **2018**, *8*, 1801418.
- (96) Zhu, L.; Zhang, M. J.; Yang, L. X.; Zhou, K. X.; Wang, Y.; Sun, D.; Tang, Y. G.; Wang, H. Y. Engineering Hierarchical Structure and Surface of $\text{Na}_4\text{MnV}(\text{PO}_4)_3$ for Ultrafast Sodium Storage by a Scalable Ball Milling Approach. *Nano Energy* **2022**, *99*, 107396.
- (97) Ghosh, S.; Barman, N.; Senguttuvan, P. Impact of Mg^{2+} and Al^{3+} Substitutions on the Structural and Electrochemical Properties of NASICON- $\text{Na}_x\text{VMn}_{0.75}\text{M}_{0.25}(\text{PO}_4)_3$ ($M = \text{Mg and Al}$) Cathodes for Sodium-Ion Batteries. *Small* **2020**, *16*, 2003973.
- (98) Hou, J.; Hadouchi, M.; Sui, L.; Liu, J.; Tang, M.; Kan, W. H.; Avdeev, M.; Zhong, G.; Liao, Y.-K.; Lai, Y.-H.; et al. Unlocking Fast and Reversible Sodium Intercalation in NASICON $\text{Na}_4\text{MnV}(\text{PO}_4)_3$ by Fluorine Substitution. *Energy Storage Mater.* **2021**, *42*, 307–316.
- (99) Lu, F. Q.; Wang, J. H.; Chang, S. Q.; He, L. H.; Tang, M. X.; Wei, Q.; Mo, S. Y.; Kuang, X. J. New-type NASICON- $\text{Na}_4\text{FeV}(\text{PO}_4)_3$ Cathode with High Retention and Durability for Sodium Ion Batteries. *Carbon* **2022**, *196*, 562–572.
- (100) Wang, S.; Zheng, J. Q.; He, L.; Zhang, L. Y.; Ge, X. C.; Li, S. H.; Wang, X.; Zhang, Z. Carbon-Modified NASICON $\text{Na}_4\text{FeV}(\text{PO}_4)_3$ Cathode with Enhanced Kinetics for High-Performance Sodium-Ion Batteries. *ACS Appl. Energy Mater.* **2022**, *5*, 9616–9624.
- (101) Ma, X. D.; Yu, X.; Li, X. W.; Liu, Q.; Liu, Y. Modulating Na Vacancies of $\text{Na}_4\text{FeV}(\text{PO}_4)_3$ via Zr-Substitution: Toward a Superior Rate and Ultrastable Cathode for Sodium-Ion Batteries. *J. Power Sources* **2022**, *541*, 231727.
- (102) Li, M.; Sun, C.; Ni, Q.; Sun, Z.; Liu, Y.; Li, Y.; Li, L.; Jin, H. B.; Zhao, Y. J. High Entropy Enabling the Reversible Redox Reaction of $\text{V}^{4+}/\text{V}^{5+}$ Couple in NASICON-Type Sodium Ion Cathode. *Adv. Energy Mater.* **2023**, *13*, 2203971.
- (103) Liu, X.; Lai, W.; Peng, J.; Gao, Y.; Zhang, H.; Yang, Z.; He, X.; Hu, Z.; Li, L.; Qiao, Y.; et al. A NASICON-typed $\text{Na}_4\text{Mn}_0.5\text{Fe}_0.5\text{Al}(\text{PO}_4)_3$ cathode for low-cost and high-energy sodium-ion batteries. *Carbon Neutralization* **2022**, *1*, 49–58.
- (104) Qi, Y.; Tong, Z.; Zhao, J.; Ma, L.; Wu, T.; Liu, H.; Yang, C.; Lu, J.; Hu, Y.-S. Scalable Room-Temperature Synthesis of Multi-

- shelled $\text{Na}_3(\text{VOPO}_4)_2\text{F}$ Microsphere Cathodes. *Joule* **2018**, *2*, 2348–2363.
- (105) Shen, X.; Zhou, Q.; Han, M.; Qi, X.; Li, B.; Zhang, Q.; Zhao, J.; Yang, C.; Liu, H.; Hu, Y. S. Rapid Mechanochemical Synthesis of Polyanionic Cathode with Improved Electrochemical Performance for Na-Ion Batteries. *Nat. Commun.* **2021**, *12*, 2848.
- (106) Wei, Y.; Zheng, M.; Zhu, W.; Pang, H. Hollow Structures Prussian Blue, Its Analogs, and Their Derivatives: Synthesis and Electrochemical Energy-Related Applications. *Carbon Neutralization* **2023**, *2*, 271–299.
- (107) Ren, J.; Zhu, H.; Fang, Y.; Li, W.; Lan, S.; Wei, S.; Yin, Z.; Tang, Y.; Ren, Y.; Liu, Q. Typical Cathode Materials for Lithium-Ion and Sodium-Ion Batteries: From Structural Design to Performance Optimization. *Carbon Neutralization* **2023**, *2*, 339–377.
- (108) Xie, B.; Sun, B.; Gao, T.; Ma, Y.; Yin, G.; Zuo, P. Recent Progress of Prussian Blue Analogues as Cathode Materials for Nonaqueous Sodium-Ion Batteries. *Coord. Chem. Rev.* **2022**, *460*, 214478.
- (109) Wang, B.; Han, Y.; Wang, X.; Bahlawane, N.; Pan, H.; Yan, M.; Jiang, Y. Prussian Blue Analogs for Rechargeable Batteries. *iScience* **2018**, *3*, 110–133.
- (110) Song, J.; Wang, L.; Lu, Y.; Liu, J.; Guo, B.; Xiao, P.; Lee, J. J.; Yang, X. Q.; Henkelman, G.; Goodenough, J. B. Removal of Interstitial H_2O in Hexacyanometallates for a Superior Cathode of a Sodium-Ion Battery. *J. Am. Chem. Soc.* **2015**, *137*, 2658–2664.
- (111) Peng, J.; Zhang, W.; Liu, Q. N.; Wang, J. Z.; Chou, S. L.; Liu, H. K.; Dou, S. X. Prussian Blue Analogues for Sodium-Ion Batteries: Past, Present, and Future. *Adv. Mater.* **2022**, *34*, 2108384.
- (112) Wang, W.; Gang, Y.; Peng, J.; Hu, Z.; Yan, Z.; Lai, W.; Zhu, Y.; Appadoo, D.; Ye, M.; Cao, Y.; et al. Effect of Eliminating Water in Prussian Blue Cathode for Sodium-Ion Batteries. *Adv. Funct. Mater.* **2022**, *32*, 2111727.
- (113) You, Y.; Yao, H. R.; Xin, S.; Yin, Y. X.; Zuo, T. T.; Yang, C. P.; Guo, Y. G.; Cui, Y.; Wan, L. J.; Goodenough, J. B. Subzero-Temperature Cathode for a Sodium-Ion Battery. *Adv. Mater.* **2016**, *28*, 7243–7248.
- (114) Guo, J.; Feng, F.; Zhao, S.; Shi, Z.; Wang, R.; Yang, M.; Chen, F.; Chen, S.; Ma, Z. F.; Liu, T. High FeLS(C) Electrochemical Activity of an Iron Hexacyanoferrate Cathode Boosts Superior Sodium Ion Storage. *Carbon Energy* **2023**, *5*, e314.
- (115) Feng, F.; Chen, S.; Zhao, S.; Zhang, W.; Miao, Y.; Che, H.; Liao, X.; Ma, Z.-F. Enhanced Electrochemical Performance of MnFe@NiFe Prussian Blue Analogue Benefited from the Inhibition of Mn Ions Dissolution for Sodium-Ion Batteries. *Chem. Eng. J.* **2021**, *411*, 128518.
- (116) Shang, Y.; Li, X.; Song, J.; Huang, S.; Yang, Z.; Xu, Z. J.; Yang, H. Y. Unconventional Mn Vacancies in Mn-Fe Prussian Blue Analogs: Suppressing Jahn-Teller Distortion for Ultrastable Sodium Storage. *Chem.* **2020**, *6*, 1804–1818.
- (117) Peng, J.; Ou, M.; Yi, H.; Sun, X.; Zhang, Y.; Zhang, B.; Ding, Y.; Wang, F.; Gu, S.; López, C. A.; et al. Defect-Free-Induced Na^+ Disorder in Electrode Materials. *Energy Environ. Sci.* **2021**, *14*, 3130–3140.
- (118) Liu, X.; Cao, Y.; Sun, J. Defect Engineering in Prussian Blue Analogs for High-Performance Sodium-Ion Batteries. *Adv. Energy Mater.* **2022**, *12*, 2202532.
- (119) Wu, X.; Wu, C.; Wei, C.; Hu, L.; Qian, J.; Cao, Y.; Ai, X.; Wang, J.; Yang, H. Highly Crystallized $\text{Na}_2\text{CoFe}(\text{CN})_6$ with Suppressed Lattice Defects as Superior Cathode Material for Sodium-Ion Batteries. *ACS Appl. Mater. Interfaces* **2016**, *8*, 5393–5399.
- (120) Sun, Y.; Xu, Y.; Xu, Z.; Sun, Y.; Xu, X.; Tu, J.; Xie, J.; Liu, S.; Zhao, X. Long-Life Na-Rich Nickel Hexacyanoferrate Capable of Working under Stringent Conditions. *J. Mater. Chem. A* **2021**, *9*, 21228–21240.
- (121) Jiang, Y.; Shen, L.; Ma, H.; Ma, J.; Yang, K.; Geng, X.; Zhang, H.; Liu, Q.; Zhu, N. A Low-Strain Metal Organic Framework for Ultra-Stable and Long-Life Sodium-Ion Batteries. *J. Power Sources* **2022**, *541*, 231701.
- (122) Xu, Y.; Ou, M.; Liu, Y.; Xu, J.; Sun, X.; Fang, C.; Li, Q.; Han, J.; Huang, Y. Crystallization-Induced Ultrafast Na-Ion Diffusion in Nickel Hexacyanoferrate for High-Performance Sodium-Ion Batteries. *Nano Energy* **2020**, *67*, 104250.
- (123) Xu, Y.; Wan, J.; Huang, L.; Xu, J.; Ou, M.; Liu, Y.; Sun, X.; Li, S.; Fang, C.; Li, Q.; et al. Dual Redox-Active Copper Hexacyanoferrate Nanosheets as Cathode Materials for Advanced Sodium-Ion Batteries. *Energy Storage Mater.* **2020**, *33*, 432–441.
- (124) Peng, J.; Zhang, W.; Hu, Z.; Zhao, L.; Wu, C.; Peleckis, G.; Gu, Q.; Wang, J. Z.; Liu, H. K.; Dou, S. X.; et al. Ice-Assisted Synthesis of Highly Crystallized Prussian Blue Analogues for All-Climate and Long-Calendar-Life Sodium Ion Batteries. *Nano Lett.* **2022**, *22*, 1302–1310.
- (125) Yang, Y.; Liu, E.; Yan, X.; Ma, C.; Wen, W.; Liao, X. Z.; Ma, Z. F. Influence of Structural Imperfection on Electrochemical Behavior of Prussian Blue Cathode Materials for Sodium Ion Batteries. *J. Electrochem. Soc.* **2016**, *163*, A2117–A2123.
- (126) Yu, Z. E.; Cheng, H.; Lyu, Y.; Liu, Y.; Zhou, J.; Chen, R.; Guo, B. A Vacancy-Free Sodium Manganese Hexacyanoferrate as Cathode for Sodium-Ion Battery by High-Salt-Concentration Preparation. *J. Alloys Compd.* **2021**, *887*, 161388.
- (127) Hu, J.; Tao, H.; Chen, M.; Zhang, Z.; Cao, S.; Shen, Y.; Jiang, K.; Zhou, M. Interstitial Water Improves Structural Stability of Iron Hexacyanoferrate for High-Performance Sodium-Ion Batteries. *ACS Appl. Mater. Interfaces* **2022**, *14*, 12234–12242.
- (128) Ojwang, D. O.; Svensson, M.; Njel, C.; Mogensen, R.; Menon, A. S.; Ericsson, T.; Haggstrom, L.; Maibach, J.; Brant, W. R. Moisture-Driven Degradation Pathways in Prussian White Cathode Material for Sodium-Ion Batteries. *ACS Appl. Mater. Interfaces* **2021**, *13*, 10054–10063.
- (129) Wang, S.; Qin, M.; Huang, M.; Huang, X.; Li, Q.; You, Y. Organic Solvothermal Method Promoted Monoclinic Prussian Blue as a Superior Cathode for Na-Ion Batteries. *ACS Appl. Energy Mater.* **2022**, *5*, 6927–6935.
- (130) Geng, W.; Zhang, Z.; Yang, Z.; Tang, H.; He, G. Non-Aqueous Synthesis of High-Quality Prussian Blue Analogues for Na-Ion Batteries. *Chem. Commun.* **2022**, *58*, 4472–4475.
- (131) Peng, J.; Gao, Y.; Zhang, H.; Liu, Z.; Zhang, W.; Li, L.; Qiao, Y.; Yang, W.; Wang, J.; Dou, S. Ball Milling Solid-State Synthesis of Highly Crystalline Prussian Blue Analogue $\text{Na}_{2-x}\text{MnFe}(\text{CN})_6$ Cathodes for All-Climate Sodium-Ion Batteries. *Angew. Chem., Int. Ed.* **2022**, *61*, e202205867.
- (132) Brant, W. R.; Mogensen, R.; Colbin, S.; Ojwang, D. O.; Schmid, S.; Häggström, L.; Ericsson, T.; Jaworski, A.; Pell, A. J.; Younesi, R. Selective Control of Composition in Prussian White for Enhanced Material Properties. *Chem. Mater.* **2019**, *31*, 7203–7211.
- (133) Jiang, Y.; Yu, S.; Wang, B.; Li, Y.; Sun, W.; Lu, Y.; Yan, M.; Song, B.; Dou, S. Prussian Blue@C Composite as an Ultrahigh-Rate and Long-Life Sodium-Ion Battery Cathode. *Adv. Funct. Mater.* **2016**, *26*, 5315–5321.
- (134) Bu, F.; Feng, X.; Jiang, T.; Shakir, I.; Xu, Y. One Versatile Route to Three-Dimensional Graphene Wrapped Metal Cyanide Aerogels for Enhanced Sodium Ion Storage. *Chemistry* **2017**, *23*, 8358–8363.
- (135) Wang, Z.; Huang, Y.; Chu, D.; Li, C.; Zhang, Y.; Wu, F.; Li, L.; Xie, M.; Huang, J.; Chen, R. Continuous Conductive Networks Built by Prussian Blue Cubes and Mesoporous Carbon Lead to Enhanced Sodium-Ion Storage Performances. *ACS Appl. Mater. Interfaces* **2021**, *13*, 38202–38212.
- (136) Mao, Y.; Chen, Y.; Qin, J.; Shi, C.; Liu, E.; Zhao, N. Capacitance Controlled, Hierarchical Porous 3D Ultra-Thin Carbon Networks Reinforced Prussian Blue for High Performance Na-Ion Battery Cathode. *Nano Energy* **2019**, *58*, 192–201.
- (137) Qiao, Y.; Wei, G.; Cui, J.; Zhang, M.; Cheng, X.; He, D.; Li, S.; Liu, Y. Prussian Blue Coupling with Zinc Oxide as a Protective Layer: An Efficient Cathode for High-Rate Sodium-Ion Batteries. *Chem. Commun.* **2019**, *55*, 549–552.
- (138) Xu, C.; Ma, Y.; Zhao, J.; Zhang, P.; Chen, Z.; Yang, C.; Liu, H.; Hu, Y. S. Surface Engineering Stabilizes Rhombohedral Sodium

- Manganese Hexacyanoferrates for High-Energy Na-Ion Batteries. *Angew. Chem., Int. Ed.* **2023**, *62*, e202217761.
- (139) Ye, M.; You, S.; Xiong, J.; Yang, Y.; Zhang, Y.; Li, C. C. In-Situ Construction of A NaF-Rich Cathode-Electrolyte Interface on Prussian Blue toward a 3000-Cycle-Life Sodium-Ion Battery. *Mater. Today Energy* **2022**, *23*, 100898.
- (140) Li, W. J.; Chou, S. L.; Wang, J. Z.; Wang, J. L.; Gu, Q. F.; Liu, H. K.; Dou, S. X. Multifunctional Conducting Polymer Coated $\text{Na}_{1-x}\text{MnFe}(\text{CN})_6$ Cathode for Sodium-Ion Batteries with Superior Performance via a Facile and One-Step Chemistry Approach. *Nano Energy* **2015**, *13*, 200–207.
- (141) Peng, F.; Yu, L.; Yuan, S.; Liao, X. Z.; Wen, J.; Tan, G.; Feng, F.; Ma, Z. F. Enhanced Electrochemical Performance of Sodium Manganese Ferrocyanide by $\text{Na}_3(\text{VOPO}_4)_2\text{F}$ Coating for Sodium-Ion Batteries. *ACS Appl. Mater. Interfaces* **2019**, *11*, 37685–37692.
- (142) You, Y.; Wu, X.-L.; Yin, Y.-X.; Guo, Y.-G. A Zero-Strain Insertion Cathode Material of Nickel Ferricyanide for Sodium-Ion Batteries. *J. Mater. Chem. A* **2013**, *1*, 14061–14065.
- (143) Wan, M.; Tang, Y.; Wang, L.; Xiang, X.; Li, X.; Chen, K.; Xue, L.; Zhang, W.; Huang, Y. Core-Shell Hexacyanoferrate for Superior Na-Ion Batteries. *J. Power Sources* **2016**, *329*, 290–296.
- (144) Yin, J.; Shen, Y.; Li, C.; Fan, C.; Sun, S.; Liu, Y.; Peng, J.; Qing, L.; Han, J. In Situ Self-Assembly of Core-Shell Multimetal Prussian Blue Analogues for High-Performance Sodium-Ion Batteries. *ChemSusChem* **2019**, *12*, 4786–4790.
- (145) Gebert, F.; Cortie, D. L.; Bouwer, J. C.; Wang, W.; Yan, Z.; Dou, S. X.; Chou, S. L. Epitaxial Nickel Ferrocyanide Stabilizes Jahn-Teller Distortions of Manganese Ferrocyanide for Sodium-Ion Batteries. *Angew. Chem., Int. Ed.* **2021**, *60*, 18519–18526.
- (146) Luo, J.; Sun, S.; Peng, J.; Liu, B.; Huang, Y.; Wang, K.; Zhang, Q.; Li, Y.; Jin, Y.; Liu, Y.; et al. Graphene-Roll-Wrapped Prussian Blue Nanospheres as a High-Performance Binder-Free Cathode for Sodium-Ion Batteries. *ACS Appl. Mater. Interfaces* **2017**, *9*, 25317–25322.
- (147) Yang, D.; Xu, J.; Liao, X. Z.; Wang, H.; He, Y. S.; Ma, Z. F. Prussian Blue/RGO with Less Coordinated Water as Superior Cathode Material for Sodium-Ion Batteries. *Chem. Commun.* **2022**, *59*, 211–214.
- (148) Tang, Y.; Zhang, W.; Xue, L.; Ding, X.; Wang, T.; Liu, X.; Liu, J.; Li, X.; Huang, Y. Polypyrrole-Promoted Superior Cyclability and Rate Capability of $\text{Na}_x\text{Fe}[\text{Fe}(\text{CN})_6]$ Cathodes for Sodium-Ion Batteries. *J. Mater. Chem. A* **2016**, *4*, 6036–6041.
- (149) Liu, Y.; He, D.; Cheng, Y.; Li, L.; Lu, Z.; Liang, R.; Fan, Y.; Qiao, Y.; Chou, S. A Heterostructure Coupling of Bioinspired, Adhesive Polydopamine, and Porous Prussian Blue Nanocubes as Cathode for High-Performance Sodium-Ion Battery. *Small* **2020**, *16*, 1906946.
- (150) Zhang, Q.; Fu, L.; Luan, J.; Huang, X.; Tang, Y.; Xie, H.; Wang, H. Surface Engineering Induced Core-Shell Prussian Blue@ Polyaniline Nanocubes as a High-Rate and Long-Life Sodium-Ion Battery Cathode. *J. Power Sources* **2018**, *395*, 305–313.
- (151) Wang, X.; Wang, B.; Tang, Y.; Xu, B. B.; Liang, C.; Yan, M.; Jiang, Y. Manganese Hexacyanoferrate Reinforced by PEDOT Coating towards High-Rate and Long-Life Sodium-Ion Battery Cathode. *J. Mater. Chem. A* **2020**, *8*, 3222–3227.
- (152) Fu, H.; Liu, C.; Zhang, C.; Ma, W.; Wang, K.; Li, Z.; Lu, X.; Cao, G. Enhanced Storage of Sodium Ions in Prussian Blue Cathode Material through Nickel Doping. *J. Mater. Chem. A* **2017**, *5*, 9604–9610.
- (153) Wang, B.; Han, Y.; Chen, Y.; Xu, Y.; Pan, H.; Sun, W.; Liu, S.; Yan, M.; Jiang, Y. Gradient Substitution: An Intrinsic Strategy towards High Performance Sodium Storage in Prussian Blue-Based Cathodes. *J. Mater. Chem. A* **2018**, *6*, 8947–8954.
- (154) Zhang, L. L.; Chen, Z.-Y.; Fu, X. Y.; Yan, B.; Tao, H. C.; Yang, X. L. Effect of Zn-Substitution Induced Structural Regulation on Sodium Storage Performance of Fe-Based Prussian Blue. *Chem. Eng. J.* **2022**, *433*, 133739.
- (155) Chen, Z. Y.; Fu, X. Y.; Zhang, L. L.; Yan, B.; Yang, X. L. High-Performance Fe-Based Prussian Blue Cathode Material for Enhancing the Activity of Low-Spin Fe by Cu Doping. *ACS Appl. Mater. Interfaces* **2022**, *14*, 5506–5513.
- (156) Wang, Z.; Huang, Y.; Luo, R.; Wu, F.; Li, L.; Xie, M.; Huang, J.; Chen, R. Ion-Exchange Synthesis of High-Energy-Density Prussian Blue Analogues for Sodium Ion Battery Cathodes with Fast Kinetics and Long Durability. *J. Power Sources* **2019**, *436*, 226868.
- (157) Xi, Y.; Lu, Y. Electrochemically Active Mn-Doped Iron Hexacyanoferrate as the Cathode Material in Sodium-Ion Batteries. *ACS Appl. Mater. Interfaces* **2022**, *14*, 39022–39030.
- (158) Zhang, H.; Peng, J.; Li, L.; Zhao, Y.; Gao, Y.; Wang, J.; Cao, Y.; Dou, S.; Chou, S. Low-Cost Zinc Substitution of Iron-Based Prussian Blue Analogs as Long Lifespan Cathode Materials for Fast Charging Sodium-Ion Batteries. *Adv. Funct. Mater.* **2023**, *33*, 2210725.
- (159) Mullaliu, A.; Asenbauer, J.; Aquilanti, G.; Passerini, S.; Giorgetti, M. Highlighting the Reversible Manganese Electroactivity in Na-Rich Manganese Hexacyanoferrate Material for Li- and Na-Ion Storage. *Small Methods* **2020**, *4*, 1900529.
- (160) Li, W.; Han, C.; Wang, W.; Xia, Q.; Chou, S.; Gu, Q.; Johannessen, B.; Liu, H.; Dou, S. Stress Distortion Restraint to Boost the Sodium Ion Storage Performance of a Novel Binary Hexacyanoferrate. *Adv. Energy Mater.* **2020**, *10*, 1903006.
- (161) Moritomo, Y.; Urase, S.; Shibata, T. Enhanced Battery Performance in Manganese Hexacyanoferrate by Partial Substitution. *Electrochim. Acta* **2016**, *210*, 963–969.
- (162) Li, J.; He, X.; Ostendorp, S.; Zhang, L.; Hou, X.; Zhou, D.; Yan, B.; Meira, D. M.; Yang, Y.; Jia, H.; et al. Tin Modification of Sodium Manganese Hexacyanoferrate as a Superior Cathode Material for Sodium Ion Batteries. *Electrochim. Acta* **2020**, *342*, 135928.
- (163) El-Hady, D. A.; Lyu, Y.; Zhan, S.; Yang, J.; Wang, Y.; Yang, F.; Zhao, Q.; Gu, M.; Shao, M. Vacancy and Composition Engineering of Manganese Hexacyanoferrate for Sodium-Ion Storage. *ACS Appl. Energy Mater.* **2022**, *5*, 8547–8553.
- (164) Xie, B.; Zuo, P.; Wang, L.; Wang, J.; Huo, H.; He, M.; Shu, J.; Li, H.; Lou, S.; Yin, G. Achieving Long-Life Prussian Blue Analogue Cathode for Na-Ion Batteries via Triple-Cation Lattice Substitution and Coordinated Water Capture. *Nano Energy* **2019**, *61*, 201–210.
- (165) Zhu, Y.; Zhang, Z.; Bao, J.; Zeng, S.; Nie, W.; Chen, P.; Zhou, Y.; Xu, Y. Multi-Metal Doped High Capacity and Stable Prussian Blue Analogue for Sodium Ion Batteries. *Int. J. Energy Res.* **2020**, *44*, 9205–9212.
- (166) Peng, J.; Wang, J.; Yi, H.; Hu, W.; Yu, Y.; Yin, J.; Shen, Y.; Liu, Y.; Luo, J.; Xu, Y.; et al. A Dual-Insertion Type Sodium-Ion Full Cell Based on High-Quality Ternary-Metal Prussian Blue Analogs. *Adv. Energy Mater.* **2018**, *8*, 1702856.
- (167) Zhang, L.; Wei, C.; Fu, X.; Chen, Z.; Yan, B.; Sun, P. P.; Chang, K.; Yang, X. Ternary Ni-Based Prussian Blue Analogue with Superior Sodium Storage Performance Induced by Synergistic Effect of Co and Fe. *Carbon Energy* **2021**, *3*, 827–839.
- (168) Ma, Y.; Ma, Y.; Dreyer, S. L.; Wang, Q.; Wang, K.; Goonetilleke, D.; Omar, A.; Mikhailova, D.; Hahn, H.; Breitung, B. High-Entropy Metal-Organic Frameworks for Highly Reversible Sodium Storage. *Adv. Mater.* **2021**, *33*, e2101342.
- (169) Ma, Y.; Hu, Y.; Pramudya, Y.; Diemant, T.; Wang, Q.; Goonetilleke, D.; Tang, Y.; Zhou, B.; Hahn, H.; Wenzel, W.; et al. Resolving the Role of Configurational Entropy in Improving Cycling Performance of Multicomponent Hexacyanoferrate Cathodes for Sodium-Ion Batteries. *Adv. Funct. Mater.* **2022**, *32*, 2202372.
- (170) Peng, J.; Zhang, B.; Hua, W.; Liang, Y.; Zhang, W.; Du, Y.; Peleckis, G.; Indris, S.; Gu, Q.; Cheng, Z. A Disordered Rubik's Cube-Inspired Framework for Sodium-Ion Batteries with Ultralong Cycle Lifespan. *Angew. Chem., Int. Ed.* **2023**, *62*, e202215865.
- (171) Zhou, A.; Cheng, W.; Wang, W.; Zhao, Q.; Xie, J.; Zhang, W.; Gao, H.; Xue, L.; Li, J. Hexacyanoferrate-Type Prussian Blue Analogs: Principles and Advances Toward High-Performance Sodium and Potassium Ion Batteries. *Adv. Energy Mater.* **2021**, *11*, 2000943.
- (172) Wei, C.; Fu, X.-Y.; Zhang, L.-L.; Liu, J.; Sun, P.-P.; Gao, L.; Chang, K.-J.; Yang, X.-L. Structural Regulated Nickel Hexacyanoferrate with Superior Sodium Storage Performance by K-Doping. *Chem. Eng. J.* **2021**, *421*, 127760.

(173) Zhao, C.; Yao, Z.; Zhou, D.; Jiang, L.; Wang, J.; Murzin, V.; Lu, Y.; Bai, X.; Aspuru-Guzik, A.; Chen, L.; et al. Constructing Na-Ion Cathodes via Alkali-Site Substitution. *Adv. Funct. Mater.* **2020**, *30*, 1910840.

(174) Liao, J.-Y.; Hu, Q.; Zou, B.-K.; Xiang, J.-X.; Chen, C.-H. The Role of Potassium Ions in Iron Hexacyanoferrate as a Cathode Material for Hybrid Ion Batteries. *Electrochim. Acta* **2016**, *220*, 114–121.

(175) Liu, Y.; He, D.; Han, R.; Wei, G.; Qiao, Y. Nanostructured Potassium and Sodium Ion Incorporated Prussian Blue Frameworks as Cathode Materials for Sodium-Ion Batteries. *Chem. Commun.* **2017**, *53*, 5569–5572.

(176) Zhang, H.; Gao, Y.; Peng, J.; Fan, Y.; Zhao, L.; Li, L.; Xiao, Y.; Pang, W. K.; Wang, J.; Chou, S. L. Prussian Blue Analogues with Optimized Crystal Plane Orientation and Low Crystal Defects toward 450 Wh kg⁻¹ Alkali-Ion Batteries. *Angew. Chem., Int. Ed.* **2023**, *62*, e202303953.

(177) Xu, Z.; Sun, Y.; Xie, J.; Nie, Y.; Xu, X.; Tu, J.; Shen, C.; Jin, Y.; Li, Y.; Lu, Y.; et al. High-Performance Ni/Fe-Codoped Manganese Hexacyanoferrate by Scale-up Synthesis for Practical Na-Ion Batteries. *Mater. Today Sustain.* **2022**, *18*, 100113.

(178) Xu, Z.; Sun, Y.; Xie, J.; Nie, Y.; Xu, X.; Tu, J.; Zhang, J.; Qiu, L.; Zhu, T.; Zhao, X. Scalable Preparation of Mn/Ni Binary Prussian Blue as Sustainable Cathode for Harsh-Condition-Tolerant Sodium-Ion Batteries. *ACS Sustain. Chem. Eng.* **2022**, *10*, 13277–13287.

(179) Wang, W.; Gang, Y.; Hu, Z.; Yan, Z.; Li, W.; Li, Y.; Gu, Q. F.; Wang, Z.; Chou, S. L.; Liu, H. K.; et al. Reversible Structural Evolution of Sodium-Rich Rhombohedral Prussian Blue for Sodium-Ion Batteries. *Nat. Commun.* **2020**, *11*, 980.

(180) Xiao, J.; Shi, F. F.; Glossmann, T.; Burnett, C.; Liu, Z. From Laboratory Innovations to Materials Manufacturing for Lithium-Based Batteries. *Nat. Energy* **2023**, *8*, 329–339.

(181) Liu, D. Q.; Shadik, Z.; Lin, R. Q.; Qian, K.; Li, H.; Li, K. K.; Wang, S. W.; Yu, Q. P.; Liu, M.; Ganapathy, S.; et al. Review of Recent Development of In Situ/Operando Characterization Techniques for Lithium Battery Research. *Adv. Mater.* **2019**, *31*, 1806620.

(182) Liu, Q.; Meng, X.; Wei, Z.; Wang, D.; Gao, Y.; Wei, Y.; Du, F.; Chen, G. Core/Double-Shell Structured Na₃V₂(PO₄)₂F₃@C Nanocomposite as the High Power and Long Lifespan Cathode for Sodium-Ion Batteries. *ACS Appl. Mater. Interfaces* **2016**, *8* (46), 31709–31715.

(183) Li, L.; Liu, X.; Tang, L.; Liu, H.; Wang, Y.-G. Improved electrochemical performance of high voltage cathode Na₃V₂(PO₄)₂F₃ for Na-ion batteries through potassium doping. *J. Alloys Compd.* **2019**, *790*, 203–211.

(184) Su, D.; Cortie, M.; Wang, G. Fabrication of N-doped Graphene-Carbon Nanotube Hybrids from Prussian Blue for Lithium-Sulfur Batteries. *Adv. Energy Mater.* **2017**, *7*, No. 1602014.

(185) Li, X.; Jiang, S.; Li, S.; Yao, J.; Zhao, Y.; Bashir, T.; Zhou, S.; Yang, S.; Li, W.; Zhu, W.; Liu, T.; Zhao, J.; Gao, L. Overcoming the rate-determining kinetics of the Na₃V₂O₂(PO₄)₂F cathode for ultrafast sodium storage by heterostructured dual-carbon decoration. *J. Mater. Chem. A* **2021**, *9*, 11827–11838.

(186) Qiao, S.; Zhou, Q.; Ma, M.; Liu, H. K.; Dou, S. X.; Chong, S. Advanced Anode Materials for Rechargeable Sodium-Ion Batteries. *ACS Nano* **2023**, *17* (12), 11220–11252.